Received: 20 August 2016 | Accepted: 27 February 2017

DOI: 10.1111/gbi.12236

ORIGINAL ARTICLE

WILEY gebiology

Paleoecology and paleoceanography of the Athel silicilyte, Ediacaran–Cambrian boundary, Sultanate of Oman

D. A. Stolper[1] | G. D. Love[2] | S. Bates[2] | T. W. Lyons[2] | E. Young[3,4] | A. L. Sessions[1] | J. P. Grotzinger[1]

[1]Division of Geological and Planetary Sciences, California Institute of Technology, Pasadena, CA, USA

[2]Department of Earth Sciences, University of California, Riverside, CA, USA

[3]Department of Earth and Space Sciences, University of California, Los Angeles, CA, USA

[4]Institute of Geophysics and Planetary Physics, University of California, Los Angeles, CA, USA

Correspondence
D. A. Stolper, Division of Geological and Planetary Sciences, California Institute of Technology, Pasadena, CA, USA.
Email: dstolper@berkeley.edu

Present address
D. A. Stolper, Department of Earth and Planetary Science, University of California, Berkeley, CA, USA

Funding information
Division of Geological and Planetary Sciences at Caltech; NSF GRFP

Abstract

The Athel silicilyte is an enigmatic, hundreds of meters thick, finely laminated quartz deposit, in which silica precipitated in deep water (>~100–200 m) at the Ediacaran–Cambrian boundary in the South Oman Salt Basin. In contrast, Meso-Neoproterozoic sinks for marine silica were dominantly restricted to peritidal settings. The silicilyte is known to contain sterane biomarkers for demosponges, which today are benthic, obligately aerobic organisms. However, the basin has previously been described as permanently sulfidic and time-equivalent shallow-water carbonate platform and evaporitic facies lack silica. The Athel silicilyte thus represents a unique and poorly understood depositional system with implications for late Ediacaran marine chemistry and paleoecology. To address these issues, we made petrographic observations, analyzed biomarkers in the solvent-extractable bitumen, and measured whole-rock iron speciation and oxygen and silicon isotopes. These data indicate that the silicilyte is a distinct rock type both in its sedimentology and geochemistry and in the original biology present as compared to other facies from the same time period in Oman. The depositional environment of the silicilyte, as compared to the bounding shales, appears to have been more reducing at depth in sediments and possibly bottom waters with a significantly different biological community contributing to the preserved biomarkers. We propose a conceptual model for this system in which deeper, nutrient-rich waters mixed with surface seawater via episodic mixing, which stimulated primary production. The silica nucleated on this organic matter and then sank to the seafloor, forming the silicilyte in a sediment-starved system. We propose that the silicilyte may represent a type of environment that existed elsewhere during the Neoproterozoic. These environments may have represented an important locus for silica removal from the oceans.

1 | INTRODUCTION

The makeup and distribution of multicellular life as preserved in the rock record changed fundamentally across the Ediacaran–Cambrian boundary (~541 Ma). Our understanding and recognition of this change are inextricably linked to the rise in the number of mineralized metazoan fossils in the Cambrian (Valentine, 2002). However, the cause of this transition and the timing and rate of this radiation remain contentious. Some explanations favor environmental drivers for these biological changes including a large-scale change to the oxidation state of the atmosphere and oceans (as reviewed by Mills & Canfield, 2014), global-scale glaciations (Hoffman, Kaufman, Halverson, & Schrag, 1998), or true polar wander (Kirschvink & Raub, 2003). Alternatively, other explanations focus on changes between or within organisms themselves. This includes the emergence of new ecological interactions (Marshall, 2006) and new genetic innovations (Davidson & Erwin, 2009).

Despite their mechanistic diversity, these hypotheses are all plausible, not mutually exclusive, and difficult to differentiate. Additionally,

primitive metazoan clades existed in some state prior to this radiation, although how far back is argued (Antcliffe, Callow, & Brasier, 2014; Droser & Gehling, 2015). Knowledge of the environments in which early Metazoa or metazoan precursors lived is necessary to evaluate the link between environmental changes and the Cambrian "explosion" of animals (Butterfield, 2009; Mills & Canfield, 2014). Multiple lines of evidence exist for Neoproterozoic Metazoa. For example, some Precambrian fossils have been interpreted as fossilized ancient animal embryos (Cohen, Knoll, & Kodner, 2009; Xiao, Yuan, & Knoll, 2000), or, alternatively, as giant sulfur bacteria (Bailey, Joye, Kalanetra, Flood, & Corsetti, 2007). Additionally, both molecular (Gold, Grabenstatter, et al., 2016; Love & Summons, 2015; Love et al., 2009) and body fossils (Brasier, Green, & Shields, 1997; Li, Chen, & Hua, 1998; Maloof et al., 2010; Yin et al., 2015) have been interpreted to indicate the presence of sponge-grade organisms in the Neoproterozoic. However, the interpretation of some of these fossils has been questioned (Antcliffe et al., 2014). Finally, some Ediacaran biota are thought to represent early animals (e.g., Kimberella; Droser & Gehling, 2015; Fedonkin & Waggoner, 1997). Many of these Ediacaran organisms are thought to have lived at or near the sediment–water interface (Xiao & Laflamme, 2009). Thus, the geochemistry (e.g., oxidation state) of the benthic environments in which these organisms lived (Canfield et al., 2008) is fundamental to our understanding of the evolution and expansion of crown-group Metazoa.

We investigated the chemical conditions and molecular fossils of organisms recorded in rocks deposited at or near the Ediacaran–Cambrian boundary in Oman from the Athel Basin of the South Oman Salt Basin. We use these constraints to better understand the relationships between the environmental geochemistry and paleobiology in benthic and pelagic waters and sediments in the basin at this time. This succession of strata was selected because it correlates with units that straddle the Ediacaran–Cambrian boundary, contains high concentrations (>1 weight %) of total organic matter, and is believed to have been deposited in "deep" water (>100–200 m deep; Amthor, Ramseyer, Faulkner, & Lucas, 2005). The Athel Basin thus potentially provides constraints on environments distinct from those with shallow, well-mixed waters in the photic zone that are more commonly encountered from this time period. Critically, bitumen and kerogen organic phases from these Athel Basin rocks have yielded steranes interpreted by some to originate from demosponges (Gold, Grabenstatter, et al., 2016; Love & Summons, 2015; Love et al., 2009), which require dissolved O_2 (i.e., they are obligate aerobes). In particular, we focused on the Athel Formation (termed the Athel "silicilyte"), a silica-rich sedimentary deposit and economically important petroleum source rock. We present petrographic examinations of thin sections and data on extractable lipid biomarkers preserved in sedimentary organic matter, iron mineral geochemistry, and stable-isotope ratios of oxygen and silicon. These measurements are used to infer the relationships between the original depositional environment of the Athel Basin and the organisms it hosted.

2 | GEOLOGIC BACKGROUND

The South Oman Salt Basin (Figure 1) is part of a subsurface network of evaporite basins studied extensively because of its hydrocarbon reserves. Allen (2007), Bowring et al. (2007), and Grotzinger and Rawahi (2014) provide detailed geological reviews of the basin. We focused on the Ara Group deposited during late Ediacaran to earliest Cambrian time (Figure 2). The Ara Group consists dominantly of shallow-water carbonate units bounded by evaporites (the A0–A6 units). U-Pb dates on zircons extracted from intra-Ara ash beds range in age from 547 to 541 Ma (Amthor et al., 2003; Bowring et al., 2007). The A4 unit contains an ash bed dated at 541 ± 0.13 Ma (Bowring et al., 2007) coincident with a global carbon-isotope excursion that marks the Ediacaran–Cambrian boundary in Oman. Additionally, as will be emphasized later, these carbonates *lack* authigenic chert (Grotzinger & Rawahi, 2014; Ramseyer et al., 2013; Schröder, Grotzinger, Amthor, & Matter, 2005; Schröder, Schreiber, Amthor, & Matter, 2003). The Ara also includes the clay-rich U-Shale and Thuleilat formations (shales) and the silica-rich Athel Formation ("silicilyte"; Figure 2), which are interpreted to have formed in a deeper-water setting compared to the carbonates. These formations as well as the Ara carbonates are encased in evaporite salts. The U-Shale is correlated in time to the A4 carbonate based on a shared high gamma-ray log character (Amthor et al., 2005). These facies are localized within a partly fault-bounded basin or "trough" (Amthor et al., 2005) referred to as the Athel Basin. Consequently, the Ara shales and silicilyte were likely deposited at or within a few million years of the Ediacaran–Cambrian boundary.

Amthor et al. (2005) estimated the water depth of the Athel sediments at the time of deposition to have been greater than 100–200 m. Deposition occurred in a fault-bounded basin relative to a co-eval platform carbonates. This interpretation is independently supported by the existence of shales and laminated quartz in the Athel Basin—such sediments are generally formed in low-energy depositional environments (e.g., below wave base). Additionally, the Athel silicilyte facies is up to 400 m thick and is thus most easily interpreted to have formed in a deep trough (Amthor et al., 2005).

The silicilyte represents a potentially unique facies in the geological record. Although classified as a chert (Amthor et al., 2005), it is unlike most mid- and late Proterozoic cherts. For example, unlike these other cherts, the silicilyte silica did not replace pre-existing minerals. Additionally, and again unlike most mid- and late Proterozoic cherts, in hand sample the silicilyte is laminated and friable. It is dominated by quartz, which is, on average, 85% of the rock by weight (Amthor et al., 2005)—other minor phases include organic carbon, smectite/illite clays, apatite, pyrite, and dolomite (Amthor et al., 2005). Clay contents of the silicilyte are typically ~4–6% by weight of the rock and organic carbon 2–5% (Al Rajaibi, Hollis, & Macquaker, 2015). Additionally, and most importantly, the silicilyte did not form in a shallow, evaporitic setting as is the case for nearly all authigenic cherts from this time period (Maliva, Knoll, & Simonson, 2005).

Multiple hypotheses have been proposed to explain the origin of the silicilyte. For example, the possibility of silica precipitation by a silica-secreting organisms has been explored but ultimately rejected based on silicon isotopic measurements (Amthor et al., 2005; Ramseyer et al., 2013). Alternatively, the passive nucleation of silica on floating microbial mats at the chemocline in the water column (Al Rajaibi et al., 2015; Amthor et al., 2005) has been proposed. Still other

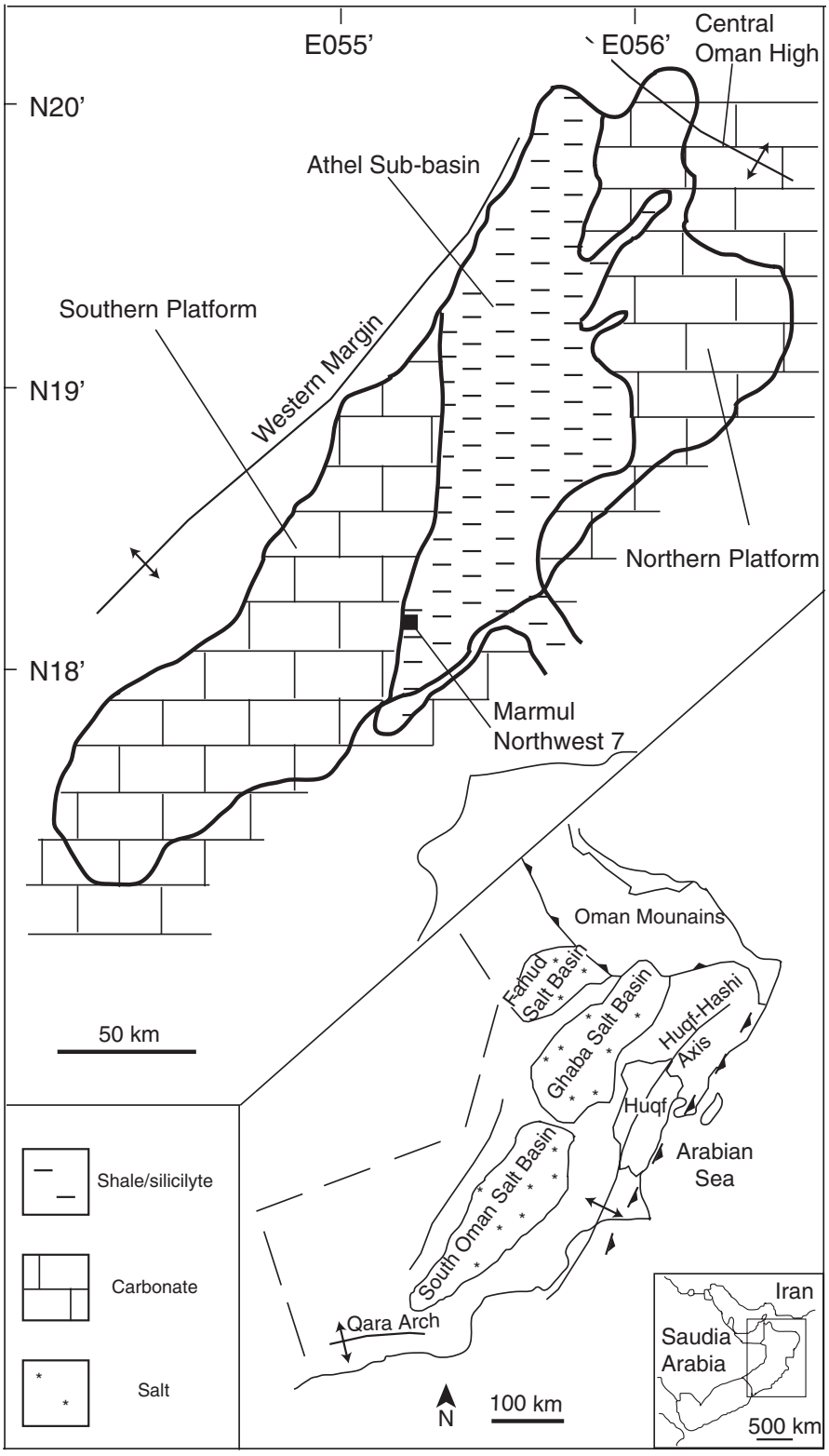

FIGURE 1 Geological map of the study area. Bottom right panel is a geographic map of the region. The central map shows the placement of the South Oman Salt Basin within Oman. The upper left panel shows in detail the South Oman Salt Basin including the location of the main well studied here, Marmul Northwest 7. Based on Amthor et al. (2005) and Schröder and Grotzinger (2007)

models favor inorganic precipitation of opal in the water column due to oversaturation of opal induced by evaporite dissolution (Ramseyer et al., 2013).

All previous studies have argued that the water column in the Athel Basin was permanently reducing and likely sulfidic (Al Rajaibi et al., 2015; Amthor et al., 2005; Ramseyer et al., 2013; Schröder & Grotzinger, 2007; Wille, Nägler, Lehmann, Schröder, & Kramers, 2008). Indeed, the presence of a chemocline and pycnocline in the water column were necessary conditions in the models of silica nucleation discussed above. Yet, biomarkers interpreted by some to indicate the presence of obligately aerobic, benthic demosponges, albeit with dissolved oxygen requirements as low as ~1% of modern

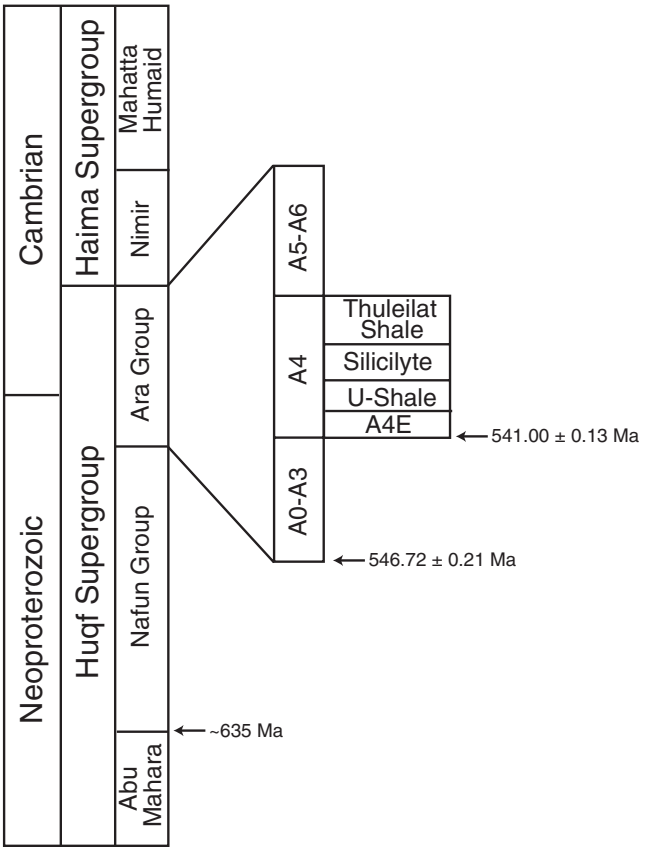

FIGURE 2 Stratigraphic column of units of interest. Ages come from ash layers within each unit (Amthor et al., 2003; Bowring et al., 2007)

air-saturated seawater values (Mills et al., 2014), are found in rocks from the Athel Basin (Grosjean, Love, Stalvies, Fike, & Summons, 2009; Love et al., 2009). Any interpretation about the paleoecology of the silicilyte requires an integrated, self-consistent model for the generation of the sediments and origin of the biomarkers preserved in those sediments. Such a model should also consider the lack of silica in the time-equivalent Ara carbonates.

3 | METHODS

3.1 | Sample preparation and extraction

Samples used for biomarker analyses are listed in Tables 1–3. Biomarker measurements were taken on cuttings (pulverized rock extracted during drilling from known depths) obtained from the Marmul NW-7 core (MMNW-7; Figure 1). Samples for biomarkers were processed according to the following procedure: Cuttings were pre-washed in water and then methanol for 1 min, vacuum-filtered, and finally rinsed briefly with dichloromethane (DCM) to remove any surface contamination. Samples were then dried and subsequently crushed by hand in a solvent-cleaned ceramic mortar and pestle (pre-solvent washed). Following this, ~2 g of each sample were extracted twice in 95:5 v/v DCM:methanol at 100°C in a CEM Mars 5 microwave extractor in pre-solvent-washed Teflon tubes. Insoluble sediment residues were separated from extracts via vacuum filtration. Elemental sulfur was removed from samples by passing extracts through copper columns activated with 1 M HCl. Asphaltenes were precipitated from maltenes with an excess of *n*-hexane solvent. Saturated, aromatic, and polar compounds were separated on activated silica gel (40–60 μm, pre-heated overnight at ~220°C) first with pure hexane, followed by 9:1 v/v hexane:DCM, and finally 95:5 v/v DCM:methanol.

TABLE 1 Rock-Eval parameters. All samples are from cuttings

Depth (m)	Formation	TOC (wt%)[a]	HI[b]	OI[c]	T_{max} (°C)
2,537	T[d]	9.0	685	8	432
2,565	T	8.8	647	10	430
2,595	T	4.0	347	23	409
2,612	T	2.3	315	52	424
2,627	S[e]	2.6	481	29	412
2,642	S	1.8	575	13	418
2,655	S	2.5	597	14	416
2,688	S	2.5	614	15	421
2,737	S	1.8	558	30	422
2,762	S	2.0	643	103	423
2,797	S	1.3	536	24	419
2,812	S	1.6	620	25	408
2,827	U[f]	2.4	220	34	410
2,860	U	3.4	452	33	417
2,887	U	7.6	398	20	430

[a]Total organic carbon.
[b]Hydrogen index.
[c]Oxygen index.
[d]Thuleilat Shale.
[e]Athel silicilyte.
[f]U-Shale.

3.2 | Lipid biomarker and Rock-Eval analyses

Samples were initially examined on a gas-chromatograph quadrupole mass spectrometer (GC-MS; Thermo Trace—DSQ) at Caltech. 1 μl of sample was injected from a programmable temperature vaporization injector in splitless mode and transferred at 350°C to a DB-5 ms or ZB-5 ms capillary column (30 m × 0.25 mm i.d. × 0.25 μm film thickness) with He as the carrier gas, heated at 20°C/min from 80 to 130°C, then 5°C/min to 320°C, and held for 20 min. *n*-alkane and mid-chain monomethylalkane relative abundances were calculated by manual integration of peaks in the chromatogram.

Samples were then measured at UC Riverside on a Waters AutoSpec Premier equipped with a HP6890 GC using a DB-1MS capillary column (60 m × 0.25 mm i.d., 0.25 μm film thickness) for biomarker identification and quantification, with He as the carrier gas. Metastable reaction monitoring (MRM) GC-MS measurements were taken with a temperature program of 60°C for 2 min, heating to 320°C at 4°C/min with a final hold at 315°C for 34 min. Aliquots of the saturated hydrocarbon fractions were spiked with 50 ng of a deuterated C_{29} sterane internal standard (d_4-ααα−24-ethylcholestane) and analyzed using published

TABLE 2 Biomarker ratios. See text for details. All samples are from cuttings

Depth (m)	Formation	mg saturate/g rock	C_{24} MMA/*n*[a]	C_{35} HHI (%)[b]	(BNH[c] + TNH[d])/C_{30}H[e]	Gamma[f]/C_{30}H[e]	S[g]/H[h]	2-MHI[i]	%C_{29}[j]	%C_{28}[j]	%C_{27}[j]	i/*n* C_{30}[k]	T_s[l]/(T_s + T_m[m])	C_{31}H 22S/(22S + R)[n]	C_{29} ααα S/ααα S + R)[o]
2,537	T[p]	2.9	0.24	12	0.46	0.08	1.01	7	63	16	21	0.61	0.35	0.56	0.49
2,565	T	1.8	0.14	9	0.48	0.08	1.18	6	62	16	23	0.49	0.38	0.56	0.47
2,595	T	3.2	0.30	12	0.68	0.14	1.25	9	63	15	22	0.84	0.46	0.57	0.49
2,612	T	1.2	0.55	15	0.80	0.19	0.95	14	65	14	21	0.86	0.44	0.56	0.49
2,627	S[q]	3.4	0.69	18	0.63	0.16	1.09	13	66	16	19	0.84	0.44	0.55	0.49
2,642	S	3.4	1.37	21	1.39	0.27	1.13	18	72	12	16	1.43	0.38	0.55	0.50
2,655	S	2.7	1.30	18	1.57	0.28	1.18	15	71	12	17	1.20	0.40	0.56	0.49
2,688	S	5.3	1.54	22	1.47	0.25	0.93	18	73	13	14	1.79	0.39	0.57	0.49
2,737	S	2.9	1.33	17	2.68	0.22	0.77	15	74	12	14	1.88	0.41	0.58	0.50
2,762	S	5.8	1.09	10	1.66	0.13	0.91	11	75	11	14	1.79	0.41	0.58	0.49
2,797	S	2.8	0.95	11	0.58	0.08	1.00	12	77	11	11	1.53	0.47	0.58	0.50
2,812	S	6.0	0.48	11	0.83	0.09	1.22	10	70	13	17	1.18	0.46	0.57	0.50
2,827	U[r]	2.4	0.32	11	0.70	0.12	1.05	11	65	15	20	0.92	0.41	0.57	0.49
2,860	U	2.5	0.27	9	0.62	0.10	1.40	7	60	17	23	0.71	0.47	0.56	0.49
2,887	U	1	0.21	11	0.59	0.08	1.17	7	62	16	22	0.71	0.40	0.55	0.50

[a]C_{24} MMA/*n*-alkane.
[b]C_{35} Homohopane Index = [C_{35} αβ (22R + 22S)]/ΣC_{31-35} αβ (22R + 22S) × 100.
[c]28,30-bisnorhopane.
[d]25,28,30-trisnorhopane.
[e]C_{30} αβ-hopane.
[f]Gammacerane.
[g]Sterane = ΣC_{27-29} steranes].
[h]Hopane = ΣC_{27-35} hopanes.
[i]2-methyl hopane index = 2-methyl hopane/[2-methyl hopane + C_{30} αβ-hopane] × 100.
[j][C_i βα diasteranes, ααα and αββ steranes]/[(C_{27} + C_{28} + C_{29}) βα diasteranes, ααα and αββ steranes] × 100.
[k]24-isopropylcholestane (ααα 22R + 22S, αββ 22R + 22S)/24-*n*-propylcholestane (ααα 22R + 22S, αββ 22R + 22S).
[l]18α(H)-22,29,30 trisnorhopane.
[m]17α(H)-22,29,30 trisnorhopane.
[n]C_{31} αβ hopane 22S/(22S + R).
[o]C_{29} sterane ααα 20S/(S + R).
[p]Thuleilat Shale.
[q]Athel silicilyte.
[r]U-Shale.

MRM GC-MS methods (Grosjean et al., 2009; Love et al., 2009). The Australian Geological Survey Organization (AGSO) standard oil was used as a reference point for the retention times of common molecules. Peaks in the chromatograms were integrated manually. Typical uncertainties in hopane to sterane ratios are ±8% or less, as calculated from multiple analyses of a saturated hydrocarbon fraction from the AGSO standard oil. Reproducibility of measurements was additionally tested by running two saturated hydrocarbon fractions (samples 2626 and 2688) multiple times. In general, most biomarker ratios reported in this paper exhibit uncertainties of about 1–2% (1 standard deviation, σ). The hopanes and steranes detected in our samples are at least three orders of magnitude higher in abundance than those found in procedural laboratory blanks with combusted sand.

Rock-Eval parameters (hydrogen index, HI; oxygen index, OI; and T_{max}) and total organic carbon (TOC) measurements were made by Weatherford Laboratories on a Vinci Rock-Eval 6 instrument following Lafargue, Marquis, and Pillot (1998) for Rock-Eval parameters and on a LECO 600 Carbon Analyzer for TOC.

3.3 | Iron speciation

Speciation among the iron minerals and total iron and aluminum contents, were determined following the methodology described in Planavsky et al. (2011) and Poulton and Canfield (2005). Concentrations of extracted iron and aluminum were measured via inductively coupled plasma mass spectrometry at UC Riverside. "Highly reactive" iron in the form of carbonate phases (principally siderite), ferric oxides (hematite in Precambrian samples), and magnetite was extracted sequentially through acid leaching. A sodium acetate solution was used initially for the carbonate-bound Fe, followed by sodium dithionite for hematite, and then ammonium oxalate for magnetite (Poulton & Canfield, 2005). Pyrite content was measured from a separate sample split via iodometric titration of sulfur released from a hot chromous chloride distillation. Pyrite iron (Fe_{Py}) content was then calculated from the measured pyrite-derived sulfur assuming a FeS_2 stoichiometry. These extracted phases are collectively referred to as "highly reactive" iron (Fe_{HR}) because they have or could have reacted with hydrogen sulfide to form pyrite during sedimentary diagenesis. Concentrations of total iron (Fe_T) and aluminum were determined on a separate aliquot of sample via a total acid digest (Planavsky et al., 2011). Reproducibility for the iron content of each sequential extraction technique is typically ~5% (Planavsky et al., 2011).

In most samples, the measured ratio of Fe_{HR}/Fe_T was found to exceed unity, with values typically between 1.04 and 1.28. Such "excesses" of highly reactive Fe are not uncommon (e.g., Clarkson, Poulton, Guilbaud, & Wood, 2014) and occur due to errors associated with the different methods used to measure the total iron vs. the sequential iron extractions. When the weight percent iron measured via the speciation extraction exceeds that in the total digest, we treat the summed Fe_{HR} data as iron total, thus ensuring all Fe_{HR}/Fe_T ratios are ≤1. The total iron content of sample 2,737 was found to be significantly lower (50%) than that of iron speciation fraction and is not discussed.

3.4 | Petrography and stable-isotope measurements

Petrographic thin sections were analyzed using both reflected and transmitted light. In addition, secondary electron microscopy (SEM), electron backscatter diffraction (EBSD), and electron-dispersive X-ray spectroscopy (EDS) maps were made at Caltech using a Zeiss 1550 VP field-emission SEM equipped with an Oxford X-Max SDD EDS system and HKL EBSD system.

Oxygen isotope ratios were measured at Caltech on a Cameca 7f secondary ion mass spectrometer (SIMS). Grains of the Caltech rose quartz standards ($\delta^{18}O$ = 8.45‰[1]) were embedded in the center of samples with epoxy, cut into thin sections, polished, and then gold-coated. Measurements were taken with a $^{133}Cs^+$ primary ion beam with a spot size of 20–30 μm. Secondary oxygen ions ($^{16}O^-$ and $^{18}O^-$) were collected via magnet hopping on a Faraday cup at a mass resolving power of ~3600. Analyses consisted of 20 cycles where ^{16}O was counted for 1 s and ^{18}O for 5 s per cycle. Average count rates were ~1×10^9 counts per second (cps) for ^{16}O and ~2×10^6 cps for ^{18}O. External precision of standards was ~0.8 ‰ (1σ).

Silicon isotope ratios (expressed as $\delta^{30}Si$) were measured via laser ablation multicollector inductively coupled plasma mass spectrometry at UCLA on a ThermoFinnigan Neptune. All methods and standards follow Shahar and Young (2007) and Ziegler, Young, Schauble, and Wasson (2010). Silicon was extracted from the sample with a 193-nm excimer laser (Photon Machines Analyte) using a 52 μm spot size. Extracted silicon was introduced to the mass spectrometer with He as the carrier gas, mixed with dry argon, and then ionized. The mass spectrometer was set to medium resolution (mass resolving power of 7,000). Instrumental mass bias (~5%) was corrected by sample-standard bracketing using a previously measured San Carlos olivine standard. Matrix effects between quartz and olivine have been shown previously to be <0.1‰ using this methodology (Ziegler et al., 2010). Accuracy was confirmed through comparison to a previously measured isotopically spiked glass. External precision was ±0.2‰ (1σ), which was determined by making 14 replicate measurements of a standard over the course of measuring samples. As in Ramseyer et al. (2013), these values are not corrected for the minor weight percent of clays in the samples. This does not influence the measurements beyond their stated precision (Ramseyer et al., 2013).

4 | RESULTS AND DISCUSSION

4.1 | Petrographic constraints on the formation of the silicilyte

Petrographic thin sections were made and examined for all samples used for geochemical analyses. Representative thin sections from core samples of the Athel silicilyte are shown under both reflected and transmitted light (Figure 3). Laminae, usually 20–30 μm thick, are

[1] $\delta = (R/R_{std}-1) \times 1{,}000$ where $^{18}R = [^{18}O]/[^{16}O]$ and $^{30}R = [^{30}Si]/[^{28}Si]$ and "std" denotes the standard to which all measurements are referenced. For this paper, all oxygen isotope measurements are referenced to VSMOW and all silicon isotope measurements are referenced to NBS 28.

TABLE 3 Comparison of measured biomarker ratios of Athel Basin samples from various studies. See Table 2 for biomarker ratio abbreviations

Formation	Phase	Study	S/H	$\%C_{29}$	C_{30} i/n	Gamma/C_{30}H	2-MHI
Thuleilat	Bitumen[a]	Love et al. (2009)	0.6–1.3	60–73	1.3–1.6	–	–
Thuleilat	Kerogen (HyPy)[b]	Love et al. (2009)	1.0–2.5	57–65	0.7–1.2	–	–
Thuleilat	Bitumen	Grosjean et al. (2009)	–	–	–	0.1–0.3	8–16
Thuleilat	Bitumen	This study	1.0–1.3	62–65	0.5–0.9	0.1–0.2	6–14
Silicilyte	Bitumen	Love et al. (2009)	0.8–1.5	72–76	1.4–2.4	–	–
Silicilyte	Kerogen (HyPy)	Love et al. (2009)	1.5–2.1	69–75	0.7–1.1	–	–
Silicilyte	Bitumen	Grosjean et al. (2009)	–	–	–	0.1–0.2	10–15
Silicilyte	Bitumen	This study	0.8–1.3	66–77	0.8–1.9	0.1–0.3	10–18
U-Shale	Bitumen	Love et al. (2009)	0.8–1	60–66	0.8–1.4	–	–
U-Shale	Kerogen (HyPy)	Love et al. (2009)	1.2	53	1.7	–	–
U-Shale	Bitumen	Grosjean et al. (2009)	–	–	–	0.1	6–9
U-Shale	Bitumen	This study	1.1–1.4	60–65	0.7–0.9	0.1	7–11

[a]biomarkers derived from the solvent-extractable portion of the rock.
[b]biomarkers derived from the hydropyrolysis of kerogen.

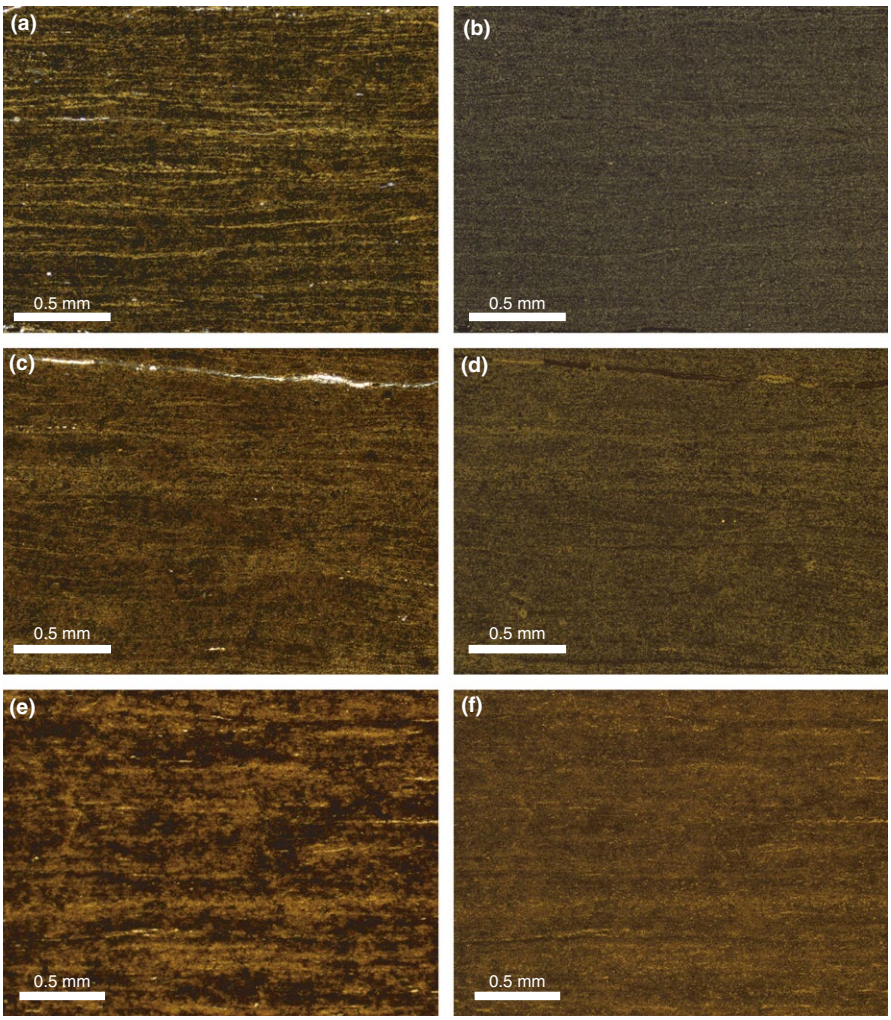

FIGURE 3 Petrographic images of samples from core. Panels on the left (a, c, and e) are transmitted light images, while those on the right (b, d, and f) are reflected. (a) and (b) are from a depth of 2,687 m, (c) and (d), 2,688 m, and (e) and (f), 2,690 m. Laminae are distinguished by differences in coloration, which reflect composition; dark regions are more organic/clay rich compared to lighter, more silica-rich layers. Laminae may be slightly wavy and discontinuous on the scale of centimeters. Additionally, laminae are variably expressed in different thin sections with, for example, (a) and (b) showing laminae more clearly than (e) and (f)

defined by differences in color (e.g. Figure 3a). Darker colors indicate larger concentrations of organic matter and/or clay. Laminae are slightly wavy and can be both continuous and discontinuous on the scale of a thin section. Additionally, pinch and swell of laminae occur. Laminae are better expressed in some samples than others, despite being only meters apart in core depth (e.g., Figure 3a and b vs. e and f). No microfossils or spicules were found in any sample, in agreement with the observations of Amthor et al. (2005).

To better understand the relationships between the silica, clay, and organic matter, samples were examined via electron-dispersive X-ray spectroscopy (EDS) and secondary electron microscopy (Figure 4). Although samples were polished before measurement, secondary electron images still show significant topography with clay/organic-rich areas being slightly recessed relative to quartz-rich areas. This difference likely occurs because clay and organic matter are softer than quartz and thus more easily removed during polishing. Silica-poor areas are either true void spaces (i.e., not an artifact of thin section preparation) or filled with organic carbon or clay (Figure 4). The clay and carbon, on the micron scale, are generally not found in the same voids. Additionally, the clay and organic matter are intimately mixed with the silica—that is, there are no distinguishable clay layers or organic layers at the micron scale. We note that samples are carbon-coated—as such, only concentrated accumulations of organic carbon (e.g., discrete kerogen particles) are discernible.

A few key observations and conclusions can be made from these petrographic examinations. First, the laminae in the silicilyte are morphologically simple. In contrast, microbial mats often create laminae with positive relief manifested by "crinkly" irregularities at the top of a lamina (e.g., as is observed in time-equivalent carbonates of the Ara; Grotzinger & Rawahi, 2014; Schröder et al., 2005) or growth features (e.g., stromatolites; Grotzinger & Knoll, 1999). Ramseyer et al. (2013) interpreted the laminae as fossilized microbial mats. Specifically, they proposed that benthic microbial mats living at the sediment–water interface captured and were encased by sedimenting silica. We argue that the silicilyte laminae lack the diagnostic features generated by microbial mats and are more consistent with simple pelagic sedimentation; we return to this in Section 5.1.

Second, laminae are defined by alternating organic carbon/clay-rich vs. carbon/clay-poor layers. Alternating laminae of differing physical properties, such as those found in varves (e.g., Thunell, Tappa, & Anderson, 1995), are often attributed to physical or chemical changes in the depositional environment due to episodic forcing such as, but not limited to, changes in seasonality, oxygenation of bottoms waters, or sediment fluxes. Previously, the layers in the silicilyte were argued to represent weekly to biweekly events (~32 laminae formed per year) by Ramseyer et al. (2013).

Third, the clay and organic content that give contrast to the laminae in the silicilyte do not form separate horizons, but instead are intimately mixed with quartz at the micron scale. The coupling of laminae to organic matter content could be the result of heterogeneous nucleation of silica on organic matter (Al Rajaibi et al., 2015; Amthor et al., 2005; Ramseyer et al., 2013), which we discuss further in Section 5.

Fourth, hand samples from core and thin sections of the silicilyte lack any discernible sedimentological hallmarks of a shallow-water depositional setting. No desiccation cracks, mud chips, or curl-up mat structures are present in any samples, nor have they been described in any previous study. This indicates that the silicilyte formed at significant water depths (>100–200 m) as opposed to in a quiet-water, shallow lagoon. Possible ripples have recently been described in the U-Shale, intermixed with plane-parallel laminations, which could indicate shallower depositional depths for the U-Shale (Al Rajaibi et al., 2015). These physical observations set critical, first-order requirements for any model of the silicilyte. That is, such a model must explain the presence of laminae, their simple morphology, sometimes discontinuous nature, and intimate association of the quartz with the organic carbon and clay.

4.2 | Biomarkers and organic parameters

The term "biomarkers," as used here, refers to fossil hydrocarbon lipids derived from ancient organisms (Brocks & Summons, 2005). Biomarker-based and Rock-Eval parameters are presented in Tables 1–3 and a selection of chromatograms in Figures 5–7. Yields of biomarkers (ng biomarker/mg saturate) are given in Table S1.

4.2.1 | Redox-sensitive biomarkers

The redox state of an environment can be recorded by a variety of biomarkers. This is because oxic conditions (i.e., dissolved O_2 is present) vs. reducing, generally sulfidic conditions (H_2S is present, dissolved O_2 is not), dictate the potential organisms that can live in a given environment. Additionally, oxic vs. sulfidic conditions control some of the diagenetic reactions that alter and ultimately preserve any organic matter remaining in the rock. We draw on three redox-sensitive biomarker-based proxies: the bisnorhopane index, the homohopane index (HHI), and the gammacerane index (Figure 8).

The biomarkers 28,30 bisnorhopane (BNH) and 25,28,30 trisnorhopane (TNH) are used as proxies for reducing, sulfidic depositional environments. BNH is hypothesized to originate from sulfide-oxidizing microbes living at the transition between sulfidic and oxic conditions (Schoell, McCaffrey, Fago, & Moldowan, 1992). TNH has been suggested to originate from a diagenetic demethylation of BNH or via direct synthesis by microbes (Peters, Walters, & Moldowan, 2005; Schoell et al., 1992). No extant source organisms for BNH or TNH are known. The ratio of BNH to C_{30} αβ hopane, known as the bisnorhopane index, is commonly used as a proxy for reducing sediments and possible water column anoxia. An index value of >0.5 (Cao et al., 2009) has been used previously to establish the presence of reducing conditions. We include the sum of BNH and TNH in the numerator of the bisnorhopane index to account for the possible diagenetic transformation of BNH to TNH. Maximum values of the index (~2.75) occur in the center of the silicilyte, while values in the U-Shale and Thuleilat are lower, averaging ~0.5 (Figure 8a). These values are consistent with the deposition of all samples in anoxic sediments and perhaps bottom waters. We note that BNH/C_{30}H ratios (~0.3–0.65) show no obvious trend through the section. Instead, the elevated (BNH + TNH)/C_{30}H values seen in the silicilyte (Figure 8a) are associated with increases in silicilyte TNH abundances. This may indicate increased demethylation of BNH to TNH in high silica conditions or a distinctive source of TNH to the silicilyte. Regardless, the higher (BNH + TNH)/C_{30}H values in the silicilyte samples relative to the bounding shales indicate that either the depositional environment of the silicilyte was more reducing than the bounding shales or had distinctive contribution of biomass from organisms that synthesize TNH precursors. Elevated BNH/C_{30}H

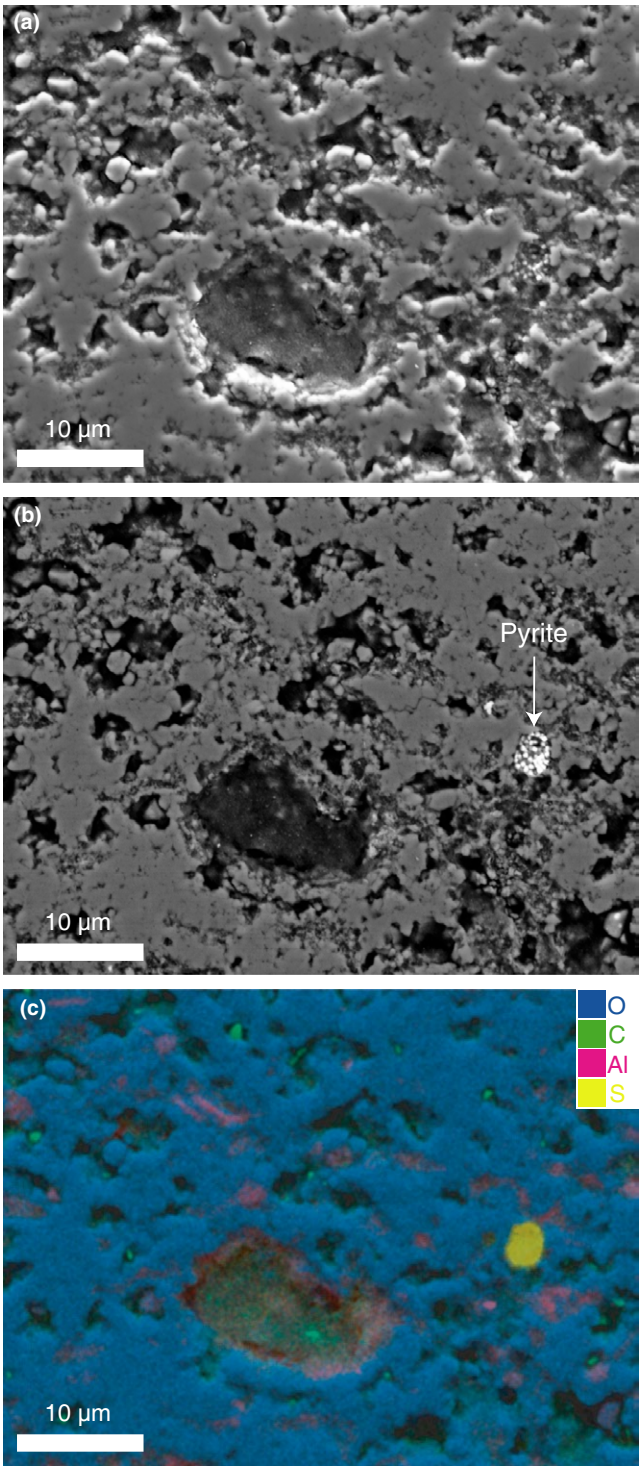

FIGURE 4 Electron microscope images from a thin section from the MMNW-7 well at 2,686.7 meters depth. (a) A secondary electron map of a representative portion of the thin section. The thin section was polished and carbon-coated before measurement. The topography, despite polishing, was generated by differential polishing of quartz compared to void spaces and clay in the rock. (b) A backscattered electron map of the same area—the large bright spots are pyrite. (c) An elemental map generated by energy-dispersive electrons. We show maps of oxygen (blue; representing silica groups), carbon (green; representing organic carbon), aluminum (red; representing clays), and sulfur (yellow; representing pyrite). Aluminum also tracks potassium concentrations indicating the presence of clays as opposed to a contaminant from polishing. Carbon and aluminum are found in void spaces between silica accumulations. Organic carbon and aluminum show no obvious association, although both are found in the large central void. Otherwise they are found separately in the smaller spaces. Organic carbon is found concentrated in small spaces throughout the sample

and TNH/C_{30}H values have been observed in all other previously studied silicilyte samples (Grosjean et al., 2009).

The homohopane index (HHI) is the percent abundance of C_{35} hopanes relative to the summed C_{31} to C_{35} hopane abundances. The HHI proxy is based on the observation that the side chains of bacteriohopanepolyols (the precursors to C_{35} hopanoids) are preferentially cleaved under oxic conditions, creating C_{31-34} hopanes. In contrast, under sulfidic conditions the side chains are thought to be stabilized via enhanced cross-linking with other organic molecules (Bishop & Farrimond, 1995; Sinninghe Damsté, Van Duin, Hollander, Kohnen, & De Leeuw, 1995). Thus, C_{35} hopane preservation is enhanced over other hopanes in sulfidic environments. Generally, HHI values in excess of 5% are interpreted to indicate reducing conditions (Cao et al., 2009). Maximum HHI values between 20 and 25% occur in the silicilyte, while the bounding shales have values near 10% (Figure 8b). This proxy indicates that the original sediments of all samples and possibly the overlying waters were at a minimum episodically anoxic and sulfidic during the time of deposition. The higher values of this ratio in the silicilyte indicate stronger reducing conditions in the original depositional environment of silicilyte as compared to the shales.

The final redox-sensitive biomarker proxy we present is the gammacerane index. This proxy employs the ratio of the abundance of gammacerane to the abundance of C_{30} αβ hopane. Its utility rests on the observation that gammacerane's precursor, tetrahymanol (Haven, Rohmer, Rullkötter, & Bisseret, 1989), is dominantly produced by ciliates living in anaerobic or microaerophilic environments at the chemocline (Haven et al., 1989). On this basis, enhanced gammacerane levels are used to infer water column stratification due to both redox- and salinity-driven gradients (Schoell, Hwang, Carlson, & Welton, 1994; Sinninghe Damsté et al., 1995). Some Proteobacteria also produce gammacerane precursors (Kleemann et al., 1990), including methylated and dimethylated forms. Thus, gammacerane, in and of itself, is not a unique biomarker for redox- or salinity-stratified waters.

Regardless, the gammacerane index reaches maximum values in the silicilyte, ranging from 0.1 to 0.3, while the bounding shales range from ~0.05 to 0.20 (Figure 8c). The increase in the gammacerane index is linked to increases in gammacerane content (as opposed to a drop in C_{30} αβ hopane content). Specifically, average values for gammacerane concentrations (ng biomarker/mg saturated extract) are 4.7× higher in the silicilyte relative to the shales, while for C_{30} αβ abundances they are 2.7× higher (Table S1). The measured gammacerane index values are not particularly elevated when compared to restricted, hypersaline depositional environments (e.g., >2; Jiamo et al., 1986). For comparison, Precambrian bitumens from a range of facies sampled in South

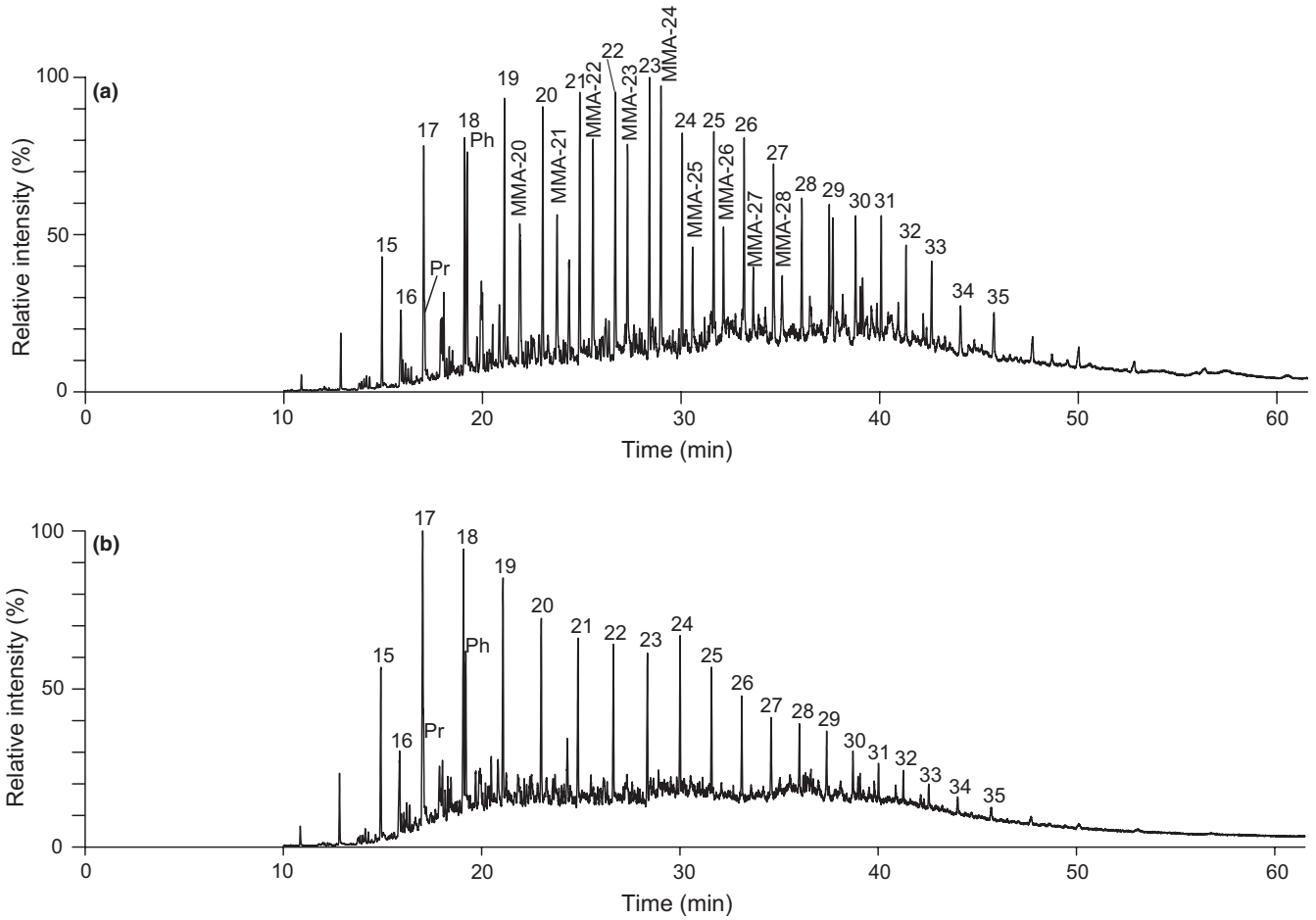

FIGURE 5 Total ion-current chromatograms of saturated hydrocarbon fractions for (a) MMNW-7 2,737 (silicilyte) and (b) MMNW-7 2,537 (Thuleilat Shale). *n*-alkanes are given by the total number of carbon atoms in the molecule, *n*. For the mid-chain monomethylalkane series, the total carbon number is given by the # in MMA-#. Note that MMAs are not single compounds but a co-elution of multiple methylalkanes with different mid-chain methylation positions. These are representative chromatograms of the shale and silicilyte samples. Pr, pristane; Ph, phytane

Oman show gammacerane index values from 0 to 0.35 (Grosjean et al., 2009). Additionally, our measured values are consistent with previous measurements of gammacerane index values from samples of the silicylite and the bounding shales (Table 3; Grosjean et al., 2009). Consequently, gammacerane index values are elevated but not exceptional in the Athel Basin relative to other Neoproterozoic formations from Oman. As such, the increase in gammacerane index values from the shales to the silicilyte, although consistent with increased restriction and possibly more reducing/saline conditions, does not signal a drastic change in the water column properties.

4.2.2 | Biomarkers indicative of their source organisms

Biomarkers are also used to infer the presence and relative abundance of organisms present in the original depositional environment (Peters et al., 2005). We present data for the 2-methylhopane index (2-MHI), $\%C_{29}$ sterane values, the sterane/hopane ratio, the 24-iso/*n*-propylcholestane (24-ipc/npc) ratio, and the C_{24} mid-chain monomethylalkane/*n*-alkane (C_{24} MMA/n) ratio (Figure 9).

The 2-MHI is a ratio of the abundance of 2α-methylhopane (a C_{31} hopanoid) to the combined abundances of C_{30} and 2α-methylhopanes. The biologically produced precursors of 2α-methylhopanes, the 2α-methylhopanoids, are sometimes attributed to a cyanobacterial source (Summons, Jahnke, Hope, & Logan, 1999). However, phylogenetic analyses by Ricci et al. (2014) demonstrate that the genes required to synthesize 2α-methylhopanoids are widespread within the Alphaproteobacteria. Furthermore, Rhizobiales Proteobacteria produce both 2α-methylhopanoids and the gammacerane precursor tetrahymanol (Rashby, Sessions, Summons, & Newman, 2007).

The highest 2-MHI values for samples from this study occur in the silicilyte and form a distinct maximum (Figure 9a). Specifically, silicilyte 2-MHI values range from 10 to 18%. In contrast, lower 2-MHI values occur in the overlying and underlying shales, ranging between 6 and 10%. The high values in the silicilyte are consistent with elevated values (15%) found in other silicilyte rocks (Grosjean et al., 2009). For comparison, Proterozoic samples often show 2-MHI values of ~5–19% (Summons et al., 1999) and values of 2–16% were measured from a range of Neoproterozoic–Cambrian rock

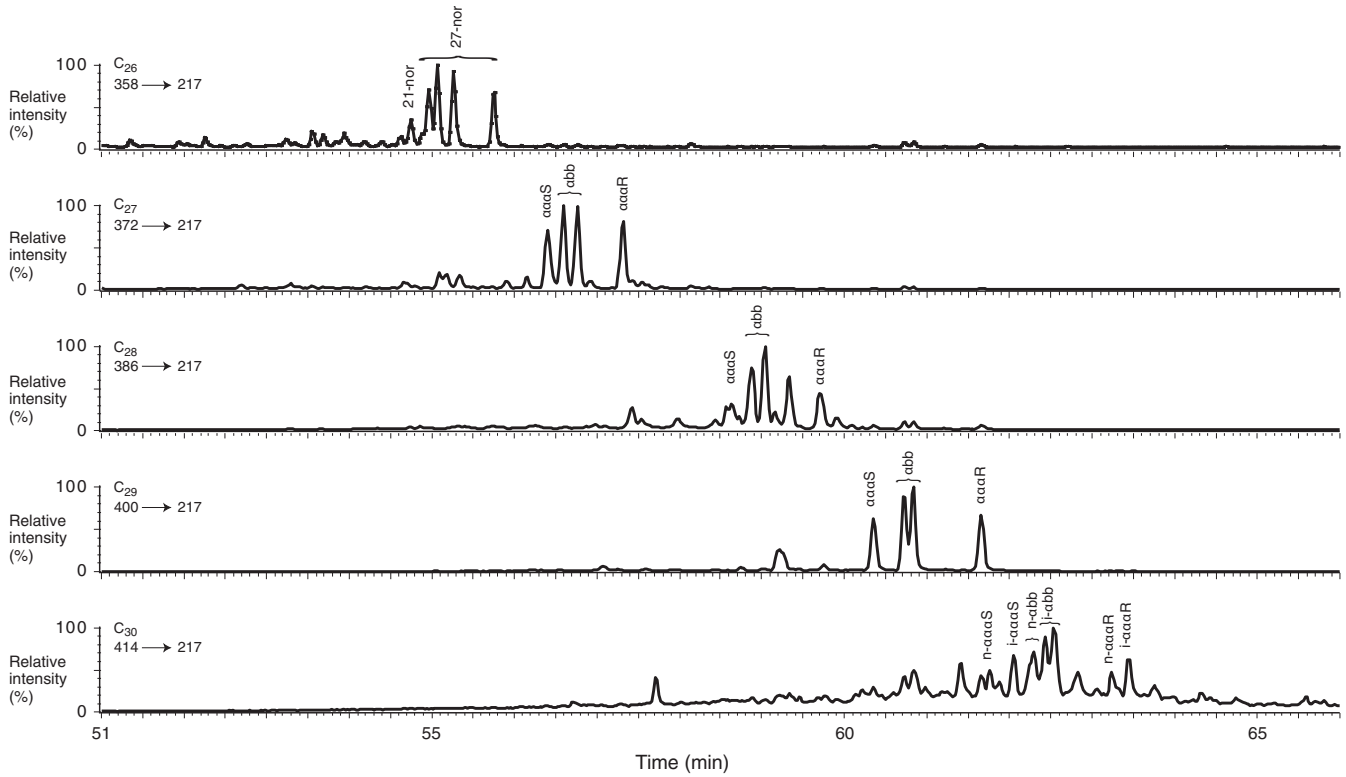

FIGURE 6 MRM GC-MS chromatograms for a selection of steranes studied. Parent to daughter transitions are given in the upper left-hand corner of the chromatograms

bitumens from South Oman (Grosjean et al., 2009). Thus, the 2-MHI ratio in the silicilyte is high both locally in Oman and globally for the Neoproterozoic. This indicates a distinct shift in the population of bacteria generating hopanoids during silicilyte deposition relative to the shales.

The $\%C_{29}$ sterane value compares the abundance of C_{29} steranes relative to the total abundance of C_{27}, C_{28}, and C_{29} steranes. It is used in Neoproterozoic- and Cambrian-aged rocks to quantify the contribution of green algae to the preserved organic matter relative to other eukaryotes (Kodner, Summons, Pearson, King, & Knoll, 2008; Volkman, Barrett, Dunstan, & Jeffrey, 1994). For this biomarker ratio, higher values indicate a larger contribution from green algae. Values for $\%C_{29}$ range from 60 to 65% in the shales and from 65 to 71% in the silicilyte (Figure 9b). For comparison, values from different Neoproterozoic facies from Oman range from 60 to 85% (Grosjean et al., 2009), and thus also show a strong C_{29} sterane predominance. These relationships suggest that the contribution of green algae relative to other eukaryotes was higher during the deposition of the silicilyte compared to the bounding shales.

The relative contribution of eukaryotic vs. bacterial biomass to the preserved sedimentary organic matter is generally inferred by using a ratio of the total abundance of C_{27}–C_{29} steranes, sourced from eukaryotes, to that of C_{27}–C_{35} hopanes, sourced from bacteria (sterane/hopane ratio; Moldowan, Seifert, & Gallegos, 1985). Sterane/hopane ratios range from ~0.8 to 1.4 in Athel samples, with a minimum observed in the silicilyte (Figure 9c). For comparison, typical sterane/hopane ratios from Neoproterozoic rocks in Oman range from 0.2 to 2.1 (Love et al., 2009). These values imply that bacteria increased in abundance relative to eukaryotes during the deposition of the silicilyte vs. the bounding shales.

The presence and abundance of 24-isopropylcholestane (24-ipc) in preserved organic carbon have been used previously to infer the presence of adult demosponges in ancient depositional settings, including in Neoproterozoic samples (Love & Summons, 2015; Love et al., 2009; McCaffrey et al., 1994). However, alternative origins have also been hypothesized (Antcliffe, 2013; Brocks & Butterfield, 2009; Lee et al., 2013), which we discuss further below (see Section 6). The abundance of 24-isopropylcholestane is generally normalized against 24-*n*-propylcholestane (24-npc) abundances. This is the 24-ipc/npc ratio. 24-npc is used as a biomarker for marine pelagophyte algae (Love et al., 2009; Moldowan et al., 1990). Values for the 24-ipc/npc ratio range from 0.4 to 0.8 in the shales and 0.6 to 1.9 in the silicilyte (Figure 9d). Importantly, nearly all samples exceed the previously established 24-ipc/npc ratio baseline value of 0.5 proposed for the positive identification of demosponge production of 24-ipc (Love et al., 2009). This value is set to be significantly above average Phanerozoic values (0.0–0.3).

A distinct maximum in 24-ipc/npc ratios occurs in the silicilyte (Figure 9d). For comparison, 24-ipc/npc ratios from diverse Neoproterozoic bitumens from South Oman range from 0.5 to 16, with an average value of 1.5 in the Huqf Supergroup (Love et al., 2009). Based on measured abundances, the higher 24-ipc/npc ratio

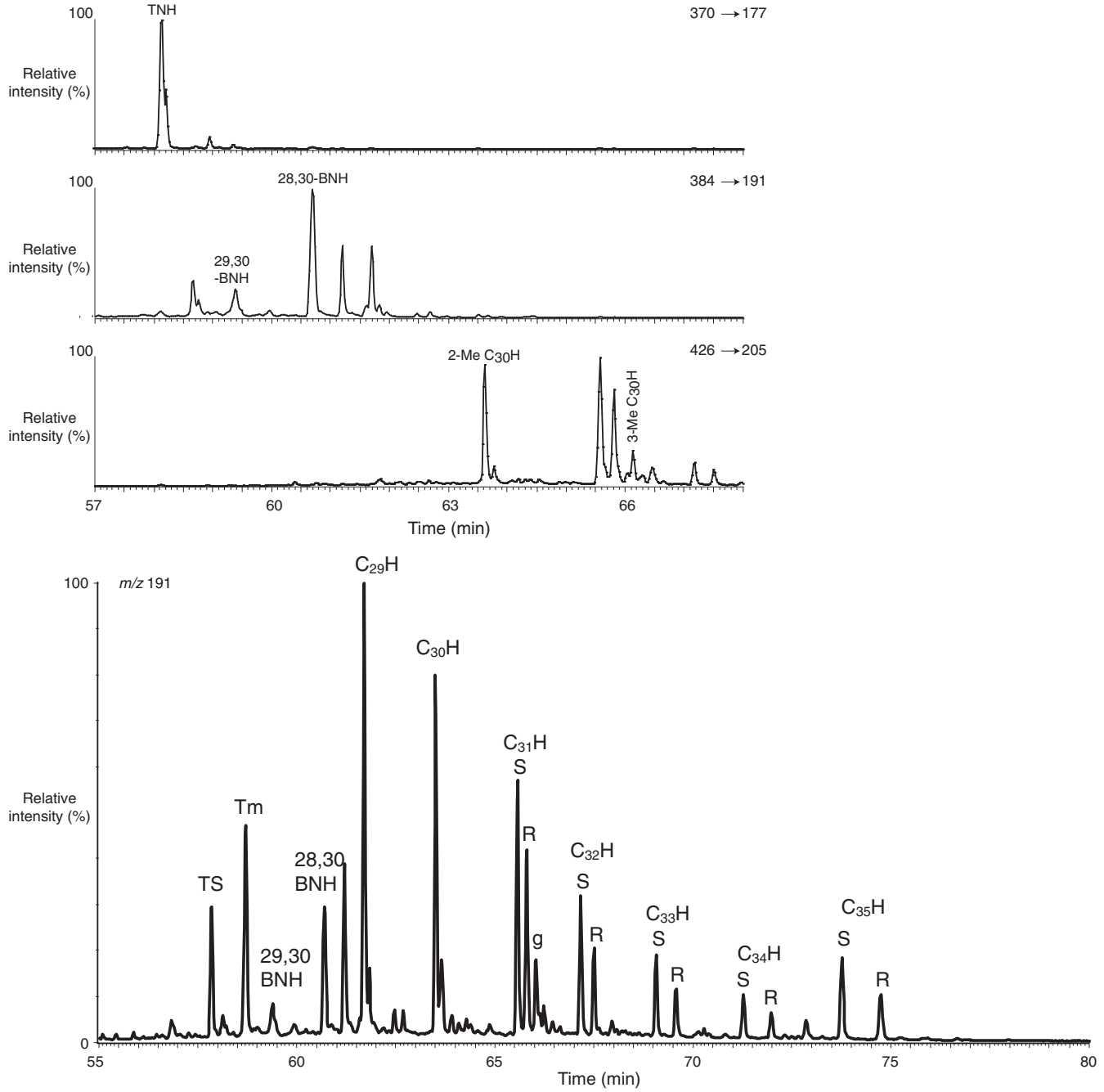

FIGURE 7 The top three panels are a selection of MRM GC-MS chromatograms for hopanes. Parent to daughter transitions are given in the upper right-hand corner of each chromatogram. The bottom panel is the combination of multiple MRM GC-MS chromatograms for a variety of major hopanoids: C_nH designates a hopanoid with n carbon atoms. T_m, 17α(H)-22,29,30-trisnorhopane; T_s, 18α(H)-22,29,30 trisnorhopane; g, Gammacerane, BNH, Bisnorhopane; TNH, trisnorhopane; 2-Me, 2 methylhopane; 3-Me, 3 methylhopane

in the silicilyte samples could not be attributed simply to a drop in the absolute abundance of 24-*n*-propylcholestane (Table S1). Specifically, the abundance of 24-ipc (ng 24-ipc/mg saturates) is 3.5 times higher on average in the silicilyte than in the Thuleilat shale and U-Shale.

A less well-constrained, but distinctive (and unusual) group of alkane biomarkers found in the silicilyte, Thuleilat shale, and U-Shale is a series of mid-chain monomethylalkanes (MMAs) with carbon numbers ranging from C_{14} through C_{30}. These MMAs are sometimes colloquially referred to as "x-peaks" and are abundant only from the late Neoproterozoic through early Ordovician (Bazhenova & Arefiev, 1996; Fowler & Douglas, 1987; Grantham, 1988; Grosjean et al., 2009; Kelly, Love, Zumberge, & Summons, 2012; Klomp, 1986; Peters, Clark, Gupta, McCaffrey, & Lee, 1995). They are particularly common in Ediacaran–Early Cambrian rocks. Although their origins are unknown, these MMAs have been proposed to be biologically sourced (Summons, Powell, & Boreham, 1988). We focus on the C_{24} MMA homolog and report its abundance relative to the C_{24} *n*-alkane (C_{24} MMA/*n* ratio).

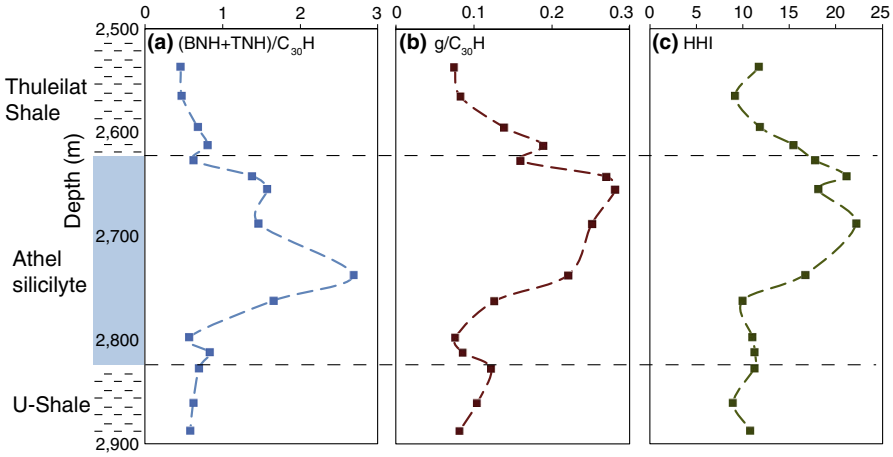

FIGURE 8 Biomarker ratios vs. stratigraphic height for redox-influenced indices. See Section 4.2.1 for details. (a) Bisnorhopane and trisnorhopane abundances relative to C_{30} hopane abundances. (b) Gammacerane abundances relative to C_{30} hopane abundances. (c) The homohopane index. These biomarker ratios indicate that the entire system was reducing in the sediments and possibly deeper in the water column below the mixed layer with the silicilyte a more reducing/stratified environment than the bounding shales

The distinctive MMA series are present in all rock bitumens analyzed in this study. The lowest C_{24} MMA/*n* ratios occur in the shales, which range in C_{24} MMA/*n* values from 0.2 to 0.3 (Figure 9e). The silicilyte, in contrast, has exceptionally elevated values ranging from 0.5 to 1.5 (Figure 9e). For comparison, C_{24} MMA/*n* ratios in Precambrian bitumens from Oman range from 0.1 to 1.7, with the highest values consistently occurring in other silicilyte samples (Grosjean et al., 2009). MMAs can make up significant portions (tens of percent) of the alkanes in these samples (Figure 5a). This implies that the organisms producing MMA precursors contributed a significant portion (of order 10%) of biomass to the preserved sedimentary organic matter.

Use of MMAs to infer past environmental conditions or the organisms present in an ancient environment is challenging due to their poorly understood origins. Specifically, no living organism has been found that produces the observed series of MMAs. Most recently, Love, Stalvies, Grosjean, Meredith, and Snape (2008) hypothesized that they are derived from bacteria living at the interface between sulfidic and oxidizing conditions within benthic microbial mats. If correct, the presence of these biomarkers would require sulfidic conditions during MMA incorporation into kerogen and a significant (10 s of percent) contribution of benthic biomass to the preserved organic carbon. Such an interpretation, while speculative, is consistent with the findings of Höld, Schouten, Jellema, and Sinninghe Damsté (1999) who demonstrated that MMAs are bound to kerogen in samples from the Huqf group in Oman through carbon–sulfur bonds. Additionally, other mid-chain methyl alkane series have previously been associated with microbial mat sources (Kenig et al., 1995; Peters et al., 2005; Shiea, Brassell, & Ward, 1990). Finally, higher abundances of monomethylalkanes and dimethylalkanes relative to *n*-alkanes in Proterozoic vs. Phanerozoic rock bitumens have been used as evidence of extensive benthic bacterial mat production in middle Proterozoic marine environments (Pawlowska, Butterfield, & Brocks, 2013).

4.2.3 | Thermal maturity parameters

Biomarker ratios and Rock-Eval parameters can be used to assess the thermal history of oils and source rocks. Because samples from all three units (both shales and the silicilyte) experienced near-identical thermal histories and span only a 350 m depth range, they should contain organic matter at similar thermal maturities. Any apparent differences in maturity can be used to diagnose differences in bitumen generation and preservation due to differing source rock chemistry (e.g., clays vs. quartz lithologies) and/or contamination. We used three molecular parameters for this evaluation based on hopane and sterane side-chain epimerization (Figure 10) in addition to the Rock-Eval parameters (Table 1).

The $T_s/(T_m + T_s)$ C_{27} hopane ratio is commonly used for thermal maturity estimations. Ts is 18α(H)-22,29,30 trisnorhopane and Tm is 17α(H)-22,29,30-trisnorhopane. Because T_s is less stable than T_m at elevated temperatures, thermal maturation causes this ratio to increase (Seifert & Moldowan, 1978) up to a maximum value of 1. Measured ratios range from 0.35 to 0.45. There are no obvious differences in ratios between the silicilyte and shales or stratigraphic height. These values correspond to early oil-window thermal maturity (Peters et al., 2005).

The relative abundance of different diastereoisomers of hopanes and steranes is also used to estimate thermal maturities. We employed side-chain epimerization ratios for C_{31} αβ hopane 22S/(22S + R) ratios and C_{29} ααα sterane 20S/(S + R) ratios (Seifert & Moldowan, 1980). In both cases, the R configuration is produced exclusively by biology. During thermal maturation, the R configuration converts to the S configuration. Maximum values of 0.6 for C_{31} αβ hopane 22S/(22S + R) and 0.55 for C_{29} ααα sterane 20S/(S + R) have been established (Peters et al., 2005). The hopane ratios range from 0.54 to 0.58, and the sterane ratios range from 0.47 to 0.5. In neither case have the parameters reached the maximum potential values. They are all consistent with early–middle oil-window thermal maturity (Peters et al., 2005). No dependence on stratigraphic height or rock type is observed supporting a uniform thermal maturity through the stratigraphic interval studied.

Rock-Eval parameters (see Section 3.2) also reflect organic matter sources and maturity. T_{max} (i.e., the temperature of maximum generation of hydrocarbons from kerogen breakdown during Rock-Eval pyrolysis) ranges for all samples are similar (~408–432°C; Table 1) and indicate the samples are of a thermal maturity lower than peak oil-window thermal maturity (Peters, 1986), in agreement with the data of Grosjean et al. (2009), and thus consistent with the early–middle oil-window thermal maturities derived from the biomarker data.

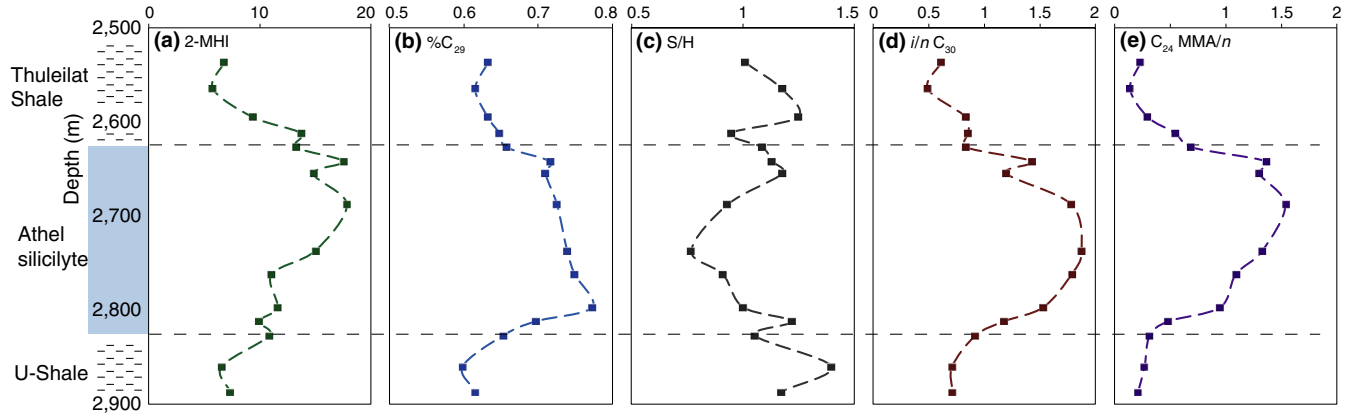

FIGURE 9 Biomarker ratios vs. stratigraphic height for biomarkers related to source organismal inputs. See Section 4.2.2 for details. (a) The 2 methylhopane index. (b) Percent abundances of C_{29} steranes relative to the sum of C_{27-29} steranes. (c) Sum of C_{27-29} sterane abundances relative to the sum of C_{27-35} hopane abundances. (d) 24-isopropylcholestane abundance relative to 24-*n*-propylcholestane abundance. (e) Abundance of C_{24}-mid-chain monomethylalkane series relative to C_{24} *n*-alkane abundance

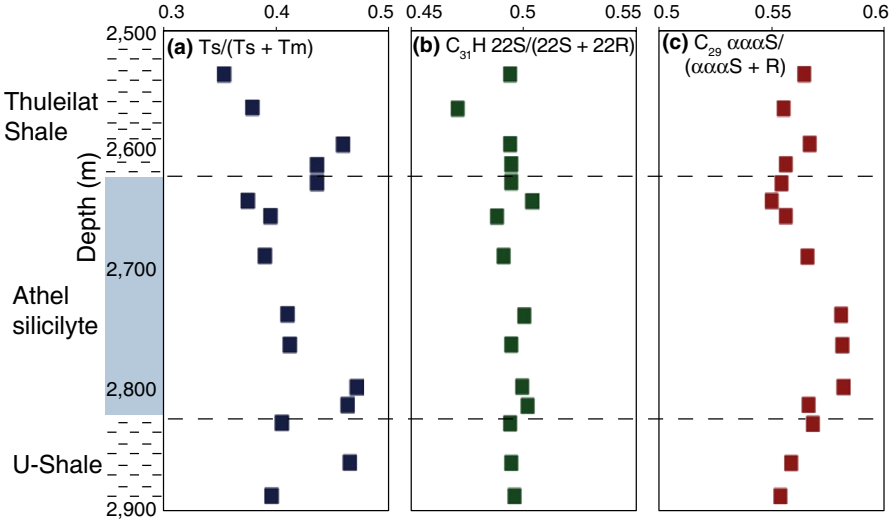

FIGURE 10 Biomarker ratios vs. stratigraphic height for maturity related biomarkers. See Section 4.2.3 for details. (a) Relative abundance of T_s [18α(H)-22,29,30 trisnorhopane] relative to the summed abundance of T_s and T_m [17α(H)-22,29,30-trisnorhopane]. (b) Relative abundance of C_{31} 22S hopanoids vs. the summed abundance of 22S and 22R configurations. (c) Relative abundance of C_{29} ααα S hopanoids vs. the summed abundance of ααα S and ααα R configurations. These biomarker ratios indicate that the shales and silicilyte are all the same thermal maturity, within the early to middle oil window

4.2.4 | Biomarker origins

The key observation from the biomarker ratios and hydrocarbon profiles is that the silicilyte and bounding shales differ markedly in their organic biomarker assemblages other than for the thermal maturity parameters. The differences in biomarker profiles between formations are stratigraphically systematic (Figures 8 and 9). However, a critical question is whether these differences result from original differences in the environment and biological communities present during deposition of the sediments or are instead the result of either facies-dependent diagenetic alteration, contamination from drilling or laboratory analysis, or contamination from flow of an organic phase through the units before drilling.

Differential alteration between the silicilyte and shale units is unlikely because the biomarker-based thermal maturity parameters, which are also sensitive to alteration (e.g., clay catalysis; Rubinstein, Sieskind, & Albrecht, 1975), are identical within error in all samples.

Contamination from both post-depositional organic migration and sampling, extraction and processing is a serious concern for all biomarker studies. Laboratory contamination is unlikely given the distinctive nature of the biomarkers and the typical low procedural blanks found for combusted sand. For example, the presence of abundant mid-chain monomethylalkanes found in the silicilyte, the overall elevated $\%C_{29}$ sterane contents, and the presence of elevated 24 ipc/npc ratios are distinctive traits Neoproterozoic to early Cambrian rocks. Such biomarkers and biomarker ratio values are not observed in routine laboratory contaminants or typical drilling fluids (Love & Summons, 2015).

Furthermore, these ratios are consistent with previous biomarker measurements made on different Athel Basin rocks processed and measured in other laboratories. This includes measurements of both bitumen and biomarkers released by the laboratory-based hydropyrolysis of kerogen (Table 3; Grosjean et al., 2009; Love, Snape, Carr, & Houghton, 1995; Love et al., 2008). Measurements of biomarkers released from kerogen are less susceptible to contamination during laboratory preparation and analysis or via flow of organic phases through emplaced sections (Love et al., 2008). Based on this, the similarity of biomarker ratios from bitumen and kerogen in Athel Basin rocks was

argued previously to demonstrate that the biomarkers extracted from bitumen were original to the sedimentary environment (Love et al., 2009). Measured values of biomarker ratios reported in this study overlap those presented in Love et al. (2009) for biomarkers measured from bitumen and released through hydropyrolysis from kerogen in the Thuleilat Shale, Silicilyte, and U-Shale (Table 3)—this is discussed more extensively below. We additionally screened samples for suspicious molecular features indicative of geologically younger inputs (e.g., biomarkers related to angiosperms, of which there are none). As such, we conclude the biomarkers are not contaminants derived during drilling or laboratory analysis.

An alternative means for contamination is the migration of organic phases (e.g., oil) through the formations studied. Biomarkers from such an exogenous source could be left behind in the formations. Multiple lines of evidence indicate that such a process is unlikely to have influenced our measured ratios:

1. All sections are encased in impermeable salt (Amthor et al., 2005), and not in contact with other units. This salt barrier prevents migration of exogenous oils at depth after the salts isolated the units.
2. The permeability of the silicilyte is low and requires extensive hydraulic fracturing to induce sufficient permeability for oil extraction. Such low permeability makes migration of other oils into the unit difficult post-lithification.
3. Introduction of exogenous biomarkers from oil migration through the units would be expected to smooth out any originally present gradients in biomarker ratios between units or as a function of depth. However, as discussed, distinctive, coherent trends and strong differences in biomarker ratios are seen not only between the silicilyte and bounding shales, but also within the specific formations themselves (e.g., Figures 8 and 9). Furthermore, our measured biomarker ratio values are consistent with those measured previously on samples from these formations (Table 3; Grosjean et al., 2009; Love et al., 2008; Love et al., 2009).
4. Biomarker ratios in the units are distinctive for the time period (the late Neoproterozoic), including the presence of the discussed series of mid-chain methyl alkanes, high $\%C_{29}$ sterane ratios, and high 24-ipc/npc ratios (Grantham, 1988; Grosjean et al., 2009; Kelly et al., 2012; Love & Summons, 2015; Love et al., 2009; McCaffrey et al., 1994; Peters et al., 1995, 2005). Phanerozoic oils would be unlikely to introduce biomarkers with these characteristics.
5. Biomarker ratios derived from the kerogen-bound biomarker pool through hydropyrolysis of kerogen from other Athel shale and silicilyte samples—as discussed above, a method that is less susceptible to contamination by migrated hydrocarbons—show similar differences between the shales and silicilyte as do the measurements of bitumens (Table 3). Specifically, the range of values we observed are in general agreement with previously measured values in both the solvent-extractable and kerogen phases of these formations penetrated by other wells (Table 3). This includes the MMAs, $\%C_{29}$ steranes, steranes–hopane ratios, gammacerane/C_{30}H ratio, 2-methyl hopane index, and C_{30} ipc/npc ratio (Table 3; Grosjean et al., 2009; Love et al., 2008; Love et al., 2009). This overlap strongly supports the presence of these biomarkers (or their precursors) in the original sediments.
6. Finally, saturate yields are typically 1–6 mg/g rock in all samples (Table 2). These yields are consistent with the relatively low thermal maturity and moderate to high organic matter content of our samples and are orders of magnitude higher than Archean samples where contamination is of key concern (Brocks, Logan, Buick, & Summons, 1999). Contamination that influences the measured ratios is more difficult in such organic-rich, low thermal maturity rocks.

Consequently, although contamination can never be completely ruled out, there is no evidence to indicate the presence of contamination and significant evidence through these self-consistency checks in support of the measured biomarkers being indigenous. Thus, we proceed below following this interpretation.

4.2.5 | Implications of the biomarker results

All biomarker parameters related to source inputs and the geochemical conditions of the depositional environment exhibit similar, first-order trends: Measured ratios or parameters begin to change at the top of the Thuleilat Shale, reach maximum or minimum values in the middle interval of the silicilyte, and then decrease or increase in the silicilyte up to the boundary with the U-Shale. Based on the established framework for interpretations of biomarker ratios, these results suggest that the depositional environment of the silicilyte was more reducing in the sedimentary pore waters and/or in the water column than in the shales and had a change in the organisms contributing to the preserved organic matter relative to the shales.

A concentrated effort to identify biomarkers for photic zone euxinia in the aromatic hydrocarbon fraction (e.g., isorenieratane or other aryl isoprenoids) was unsuccessful. This has been the case for other Neoproterozoic–Cambrian rocks in South Oman (Grosjean et al., 2009) and suggests that a water column chemocline, if present, was below the photic zone. Importantly, anoxic conditions deeper in the water column do not preclude the presence of cyanobacteria or green algae (as indicated by the biomarker measurements) in a shallower and oxic photic zone.

4.3 | Iron speciation

To further characterize the redox state of the depositional environment of the silicilyte and bounding shales, we also measured chemical speciation parameters for iron minerals in samples from MMNW-7. The distribution of iron in different mineral phases (Poulton & Canfield, 2005) is sensitive to depositional and diagenetic redox conditions and fully independent of the lipid biomarker proxies used above. The method is based on the observation that "reactive" iron is buried and preserved as either iron oxides like hematite and magnetite; iron carbonate minerals; or, if sulfide is present, as pyrite (Canfield, Raiswell, & Bottrell, 1992). Systems with high pyrite iron

TABLE 4 Iron mineral speciation results. Abundances of iron pools are given as weight percent of total rock. Ratios are weight percent/weight percent. All samples were prepared from cuttings unless noted

Depth (m)	Formation	Sodium Acetate Fe	Dithionite Fe	Oxalate Fe	Pyrite	Pyrite/Fe_{HR}[a]	Fe_{HR}/Fe_T[b]	Fe/Al[c]
2,537 #1	T[d]	0.13	0.52	0.06	1.07	0.60	–	–
2,537 #2	T	0.10	0.54	0.04	1.12	0.62	–	–
2,565	T	0.12	0.83	0.12	1.66	0.61	1.0	1.1
2,595	T	0.37	1.69	0.20	0.99	0.31		–
2,612	T	0.12	0.99	0.23	1.20	0.47	1.0	0.8
2,627	S[e]	0.07	1.20	0.42	0.41	0.20	–	–
2,642	S	0.02	0.41	0.00	0.21	0.34	1.0	1.0
2,655	S	0.06	0.52	0.01	0.33	0.36	1.0	0.9
2,688	S	0.07	0.63	0.10	0.24	0.23	1.0	1.0
2,737 #1	S	0.02	0.17	0.00	0.20	0.51	–	–
2,737#2	S	0.02	0.15	0.00	0.19	0.52	–	–
2,762	S	0.02	0.28	0.00	0.39	0.56	1.0	0.5
2,797	S	0.04	0.22	0.01	0.33	0.55	1.0	0.9
2,812	U[f]	0.04	0.43	0.03	0.28	0.36	1.0	0.5
2,827	U	0.21	1.06	0.36	1.08	0.40		–
2,860	U	0.12	1.11	0.10	1.21	0.48	1.0	0.7
2887	U	0.11	0.68	0.27	1.33	0.56	0.6	0.7
2,686 outer core	S	0.08	0.12	0.03	0.30	0.57	–	–
2,686 inner core	S	0.07	0.10	0.01	0.27	0.60	–	–

[a]Highly reactive iron is the sum of sodium acetate, dithionite and oxalated extractable iron plus pyrite iron.
[b]Total iron.
[c]Total aluminum.
[d]Thuleilat Shale.
[e]Athel silicilyte.
[f]U-Shale.

relative to total reactive iron are iron limited for pyrite generation. In such cases, free sulfide can accumulate in the pore fluids and even the water column (Poulton & Canfield, 2005; Raiswell, Buckley, Berner, & Anderson, 1988; Raiswell & Canfield, 1998). Fe_{Py}/Fe_{HR} values >0.7–0.8 are generally assumed to indicate permanently sulfidic conditions in the pore waters or the water column (Poulton & Canfield, 2011; Reinhard, Raiswell, Scott, Anbar, & Lyons, 2009). Additionally, Fe_{HR}/Fe_T and Fe_T/Al weight percent ratios are commonly elevated when the water column is anoxic relative to sediments receiving the same terrigenous material under oxic conditions. Therefore, Fe_{Py}/Fe_{HR} values >0.7 combined with Fe_{HR}/Fe_T values elevated relative to source sedimentary material are often taken as a fingerprint for water column euxinia. In contrast, low Fe_{Py}/Fe_{HR} (<0.7) but elevated Fe_{HR}/Fe_T ratios (relative to the source terrigenous material) are assumed to indicate anoxic water columns dominated by dissolved Fe(II) rather than sulfide.

Pyrite makes up between 22 and 62% of the highly reactive iron pool in the silicilyte and shale samples (Table 4; Figure 11), consistent with substantial amounts of bacterial sulfate reduction. There is no obvious relationship between facies or stratigraphic height and Fe_{Py}/Fe_{HR} values. The maximum value from the shale units is 0.62, while the silicilyte maximum value is 0.56. A potential concern with these measurements is that all samples have noticeable post-drilling oxidation, as indicated by the presence of gypsum efflorescence on core exteriors. This oxidation, if significant, could lower measured Fe_{Py}/Fe_{HR} values relative to original depositional values.

We addressed the possibility of oxidation by comparing the outside, exposed portion of a drill core from the silicilyte (as opposed to cuttings) to a freshly exposed, unoxidized surface 0.5–1 cm into the core. Fe_{Py}/Fe_{HR} values are 0.60 for the fresh interior sample and 0.57 for the exterior sample. Thus, the two measurements are similar, which indicates that oxidation during storage, at least in the cores, has negligibly altered Fe_{Py}/Fe_{HR} values. However, the lower values in other samples (as low as 0.22) may be the result of later oxidation given that cuttings have higher surface area-to-volume ratios compared to core. Regardless, ~0.6 is the maximum observed Fe_{Py}/Fe_{HR} value for both the shale and silicilyte samples. Fe_{Py}/Fe_{HR} ratios of 0.6 fall below the traditional 0.7–0.8 thresholds routinely used to indicate permanently sulfidic depositional conditions in the water column (Poulton & Canfield, 2011; Reinhard et al., 2009).

The measured Fe_{HR}/Fe_T (0.6–1.0) and Fe_T/Al (0.5–1.1) ratios are elevated relative to average Phanerozoic values for marine shales

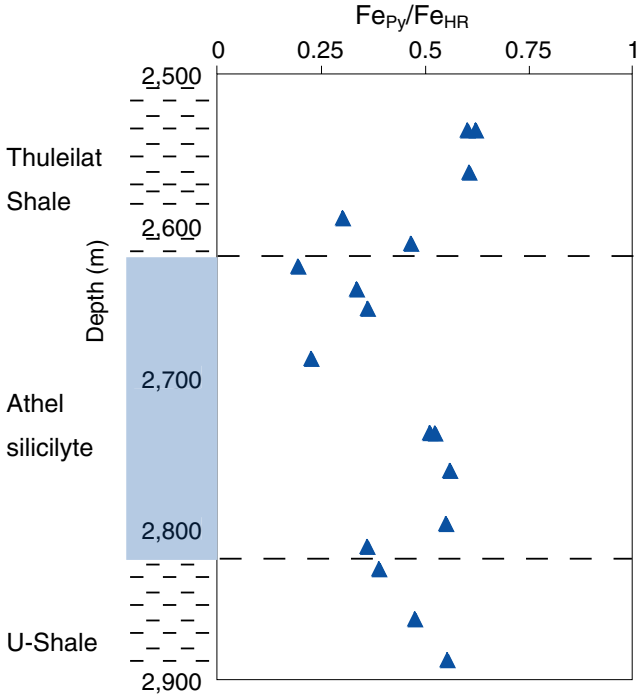

FIGURE 11 Iron speciation measurements, specifically the ratio of pyrite (Fe_{Py}) vs. highly reactive iron (Fe_{HR}), which includes the iron pool that can react with dissolved sulfide (or did react in the case of pyrite) during sedimentary diagenesis. Ratios >0.7–0.8 are generally considered to represent sulfidic environments. As all samples are below these threshold values, we interpret this to indicate that the silicilyte did not form in a persistently sulfidic (euxinic) water column

deposited in oxic environments (~<0.4 and ~0.55 ± 0.11, respectively). Following the typical interpretive framework and assuming the source sedimentary material was similar to average sources for Phanerozoic shales (Poulton & Canfield, 2011; Reinhard et al., 2009) would indicate that the water column was anoxic and contained appreciable concentrations dissolved Fe(II) rather than sulfide.

This interpretation of the iron speciation data, that is, that the water column was anoxic and contained significant amounts of dissolved Fe(II) is in disagreement with previous interpretations of the chemical conditions in the Athel Basin water column. Specifically, multiple other inorganic proxies have been used previously to argue that sulfidic conditions were present in the water column of the Athel Basin including: molybdenum isotopes (Wille et al., 2008), trace metal abundances (Al Rajaibi et al., 2015; Schröder & Grotzinger, 2007), sulfur isotopes (Schröder, Schreiber, Amthor, & Matter, 2004), and pyrite framboid size distributions (Al Rajaibi et al., 2015). Additionally, redox-sensitive biomarker ratios such as the bisnorhopane and homohopane indices discussed above are generally thought to become elevated only under sulfidic conditions.

This disagreement may result from the comparison of Fe_{HR}/Fe_T and Fe/Al ratios from the Athel Basin to values for average Phanerozoic marine shales. Specifically, knowledge of the initial Fe_{HR}/Fe_T and Fe/Al values for the source detrital materials is necessary to evaluate whether the values from the Athel Basin are actually elevated relative to the source materials. The Athel Basin was not an open marine system, but rather was a semi-enclosed basin with unknown and potentially locally controlled Fe_{HR}/Fe_T and Fe/Al values for the source siliciclastics. Thus, the high Fe_{HR}/Fe_T and Fe/Al values relative to marine shales could simply be due to source materials that were elevated relative to typical detrital inputs to marine systems. Such a case occurs today in the Mediterranean (Lyons & Severmann, 2006). Consequently, given uncertainties surrounding the background Fe_{HR}/Fe_T and Fe_T/Al ratios for a semi-enclosed basin like the Athel Basin, the iron speciation data only require, based on the ~0.6 maximum Fe_{Py}/Fe_{HR} values, significant production of sulfide in sediments and potentially intermittent sulfide accumulation in the water column. Such a conclusion is also consistent with the biomarker data and the interpretation of other inorganic redox-sensitive proxies discussed above. This is not to say that low O_2 conditions did not exist below the mixed layer in the Athel Water Column. Rather, the data indicate that anoxic, sulfidic conditions were not a permanent condition at depth in the water column. We return to the geochemical conditions of the water column in Section 5.2

4.4 | Stable isotopic composition of silica in the silicilyte

The stable isotopic composition of silica ($\delta^{18}O$ and $\delta^{30}Si$) can provide insights into silica formational and diagenetic processes (Blatt, 1987; Douthitt, 1982). We present data from silicilyte quartz for both isotopic systems.

4.4.1 | Silicon isotope ratios as a test for the spongal origin of the silicilyte

The high abundance of 24-isopropylcholestane can be interpreted to indicate demosponges lived in the Athel Basin. As some extant demosponges secrete opal spicules, sponges are a possible source of the silicilyte silica. Sponges exhibit some of the largest silicon isotopic fractionations known, precipitating opal up to 5‰ lower in $\delta^{30}Si$ than aqueous silica (Hendry & Robinson, 2012). Although the seawater $\delta^{30}Si$ value at the time of the Ediacaran–Cambrian boundary is not known, it has been estimated to be 1.3‰ (Ramseyer et al., 2013). Thus, if sponges played a key role in precipitating the silica present in the silicilyte, the $\delta^{30}Si$ value of quartz in the silicilyte is predicted to be negative.

We tested this prediction by measuring $\delta^{30}Si$ values from three different samples from the MMNW-7 core (depths of 2,687–2,690 m; Table 5). $\delta^{30}Si$ values range from ~+0.6 to +1.5‰ and are similar to the range of 0.4–1.2‰ measured by Ramseyer et al. (2013) on silicilyte rocks from other wells. These values do not have negative $\delta^{30}Si$ values as predicted above. Additionally, they are not distinct in their $\delta^{30}Si$ values from other cherts formed during this time frame (0.5 ± 1.5‰; Robert & Chaussidon, 2006). Consequently, and in accordance with the conclusion of Ramseyer et al. (2013), the silicon isotopic values are inconsistent with a spongal origin for the silica in the silicilyte.

TABLE 5 Silicon isotope results for a selection of MMNW-7 silicilyte samples obtained from drill core

Depth (m)	$\delta^{30}Si$ (‰)[a]
2,687 #1	1.23
2,687 #2	1.27
2,687 #3	1.26
2,688 #1	1.13
2,688 #2	1.07
2,688 #3	0.85
2,688 #4	0.75
2,688 #5	0.59
2,690 #1	1.46
2,690 #2	1.50

[a]Referenced to NBS-28.

4.4.2 | Oxygen isotope ratios and diagenesis in the silicilyte

Oxygen isotope ratios reflect the source and environmental conditions (e.g., temperature) of silica precipitation or later modification such as conversion from opal to quartz (Blatt, 1987; Knauth & Epstein, 1976). We measured matrix (i.e., non-fracture filling) quartz $\delta^{18}O$ ($\delta^{18}O_{qz}$) values via SIMS analyses (see Section 3.5) on samples from MMNW-7 core at depths of 2,686.7 (n = 55), 2,687.8 (n = 21), and 2,690 (n = 57) meters, where n denotes the number of spot analyses for each sample. Measurements are reported following Marin-Carbonne, Chaussidon, and Robert (2010) by treating each spot analysis as a Gaussian distribution defined by the mean and 1σ uncertainty of the measurement. The $\delta^{18}O$ frequency distribution for a given sample is found by summing the distributions for all spot analyses and then normalizing to the total number of spots measured.

$\delta^{18}O$ frequency distributions range in individual samples by ~10‰, and 12‰ across all samples (Figure 12). Samples 2,686.7 and 2,687.8 have similar peak $\delta^{18}O_{qz}$ values at ~25.5‰, while sample 2,690 has a peak value at 27‰ (Figure 12). These peak values are similar to the 24.3–28.1‰ range observed in matrix quartz reported by Ramseyer et al. (2013) on silicilyte samples from different wells using laser fluorination techniques. Our larger $\delta^{18}O_{qz}$ range of ~12‰ is likely due to the smaller (20 μm) spatial scale of SIMS vs. fluorination measurements—larger scale measurements tend to homogenize smaller-scale variations.

The $\delta^{18}O$ values can be used to calculate equilibrium formation temperatures of the quartz in water of fixed isotopic composition. Using the quartz–water isotope fractionation-factor calibration of Knauth and Epstein (1976) and a $\delta^{18}O_{water}$ of 0‰, the 10–12‰ range in $\delta^{18}O$ indicates quartz formation over a ~70°C range, with most quartz generated between 48 and 55°C. Although the oxygen isotopic composition of seawater is not well constrained for this time period (thus affecting the absolute temperature calculation), the ~70°C range is independent of this assumption and inconsistent with the initial formation or subsequent isotopic re-equilibration of the quartz or opal precursor in seawater or shallow sediments where temperature ranges of ~70°C are not found. Instead, this calculation, which assumes a constant $\delta^{18}O$ value for the formational fluid, indicates formation or isotopic re-equilibration of silicilyte quartz over depths of multiple kilometers, which would allow samples to form over a large (>50°C) temperature range.

Alternatively, ranges in $\delta^{18}O_{qz}$ can be caused by variable formation/pore-water isotopic compositions. For example, if diagenesis occurs at higher temperatures than silica precipitation, the progressive recrystallization of opal to chert can cause pore waters to evolve to higher isotopic compositions (Marin-Carbonne et al., 2010). Quartz generated from this evolving pore water will necessarily exhibit a range of isotopic compositions. For example, at the 20 μm scale Marin-Carbonne et al. (2010) observed 5–7‰ ranges in $\delta^{18}O$ in different cherts from the Gunflint Formation (1,800 Ma). These authors explained this range as the result of changes in the isotopic composition of pore waters at burial depths >2 km (assuming a 25°C geotherm)

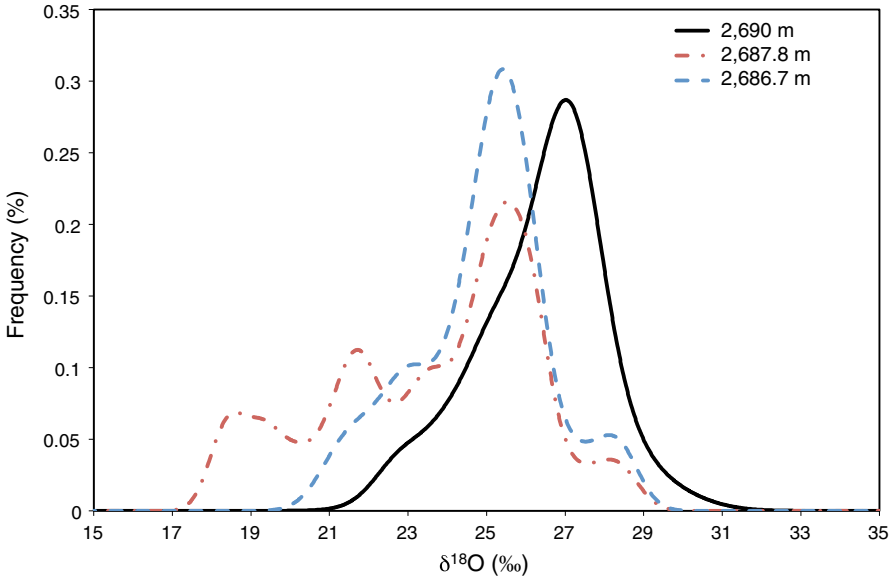

FIGURE 12 $\delta^{18}O$ data (referenced to VSMOW) measured via secondary ion mass spectrometry from three separate silicilyte core samples from MMNW-7. Measurements are treated as frequency distributions to fully represent the error of the measurements. Individual samples have a width of ~10‰ with a total range for all samples of ~12‰. This distribution indicates either a large (~70°C) range in formation temperature, or a range in the isotopic composition of the pore waters

due to progressive alteration of opal to quartz over this depth interval. Consequently, large ranges of $\delta^{18}O_{qz}$ values can also be attributed to evolving pore waters but still require conversion from opal to quartz over multiple kilometers in the sedimentary column. We note that silicon isotopes will not undergo such isotopic changes. This is because silicon dominantly occurs in silica minerals as opposed dissolved in water in silica-rich sediments. In other words, silicon has a lower water rock ratio relative to oxygen in silica-rich sediments.

Regardless of mechanism, the range in $\delta^{18}O_{qz}$ values indicates that the quartz in the silicilyte formed (or at least recrystallized from a precursor) in an evolving environmental system over multiple kilometers of depth in the sediments. The quartz is thus unlikely to be primary, but instead was likely opal that recrystallized to quartz during diagenesis. This hypothesis potentially explains features seen in the thin sections: For example, the blockier, poorly expressed laminae of some samples (Figure 3e and f) may result from deeper, later conversion of opal to quartz after compaction and dewatering have already disrupted original laminae. Thus, these features need not be explained in a model for the initial formation of the laminae in the silicilyte.

5 | MECHANISMS FOR SILICA PRECIPITATION AND A PALEOCEANOGRAPHIC MODEL FOR THE ATHEL BASIN

Here, we present a conceptual model for the formation of the silicilyte that is consistent with the observations and measurements discussed above. We first examine the possible physical and chemical conditions required for silica precipitation.

5.1 | Potential silica precipitation mechanisms

Understanding the source of silicilyte silica is critical for any model of its formation. Silica (e.g., as opal) can precipitate due to biological secretions (e.g., sponge spicules and diatom frustules) or due to silica supersaturation induced by evaporation, by pH, density, or temperature changes, or through sorption and precipitation on, for example, organic matter (i.e., templating). As discussed above, both the positive $\delta^{30}Si$ values and lack of any observed fossil spicules are inconsistent with a spongal origin for the silicilyte. A hydrothermal source for the silica was ruled out based on a rare earth element study of the silicilyte (Schröder & Grotzinger, 2007).

A critical observation is that shallow-water time-equivalent Ara carbonates lack diagenetic cherts (Grotzinger & Rawahi, 2014; Ramseyer et al., 2013; Schröder et al., 2003, 2005). In the Meso-Neoproterozoic, the major flux of silica out of the oceans is thought to have occurred due to the evaporative supersaturation of opal in shallow waters (Maliva et al., 2005). Thus, it is intriguing that the co-eval Ara carbonates, which represent a transiently evaporitic environment, lack silica. To explain this, we propose the Athel Basin acted as a filter, removing silica from incoming waters before they passed across the shallower carbonate platforms. This relationship requires silica to not only have precipitated in the Athel Basin but also to have been drawn down to sufficiently low levels that evaporation on the carbonate ramp failed to achieve sufficient silica oversaturation for opal precipitation. This, for example, makes evaporation, and large pH, temperature, or salinity changes unlikely mechanisms for silica removal in the Athel Basin. This is because neither process can lower H_4SiO_4 concentrations below the solubility limit of opal and thus prevent silica precipitation on the evaporative carbonate shelf.

Another mechanism for silica precipitation is through nucleation on organic matter (i.e., templating). It has been hypothesized that microbial cells, through silica sorption, can cause local silica oversaturation and precipitation of quartz precursors in nominally silica undersaturated waters (Fein, Scott, & Rivera, 2002). Sorption on living cells does not appear to enhance silica precipitation over abiotic rates (Fein et al., 2002; Konhauser, Jones, Phoenix, Ferris, & Renaut, 2004; Mountain, Benning, & Boerema, 2003; Yee, Phoenix, Konhauser, Benning, & Ferris, 2003). In contrast, decaying organic matter does appear to enhance silica precipitation relative to abiotic systems via interactions between exposed organic functional groups and dissolved SiO_4 (Ferris, Fyfe, & Beveridge, 1988; Knoll, 1985; Knoll & Golubic, 1979; Leo & Barghoorn, 1976). Thus, silica precipitation on organic matter debris in the water column could act as a sedimentary sink for silica. This process would require that enough silica sorbed onto organic matter to prevent silica formation on the carbonate shelves during evaporation. This scavenging could occur on floating, decaying microbial mats, as envisioned by Al Rajaibi et al. (2015) and Amthor et al. (2005), on benthic mat substrates, or simply on decaying particulate organic matter sinking through the water column.

Nucleation on intact mats floating in the water column was favored by Al Rajaibi et al. (2015) and Amthor et al. (2005) because it provides a ready explanation for the presence of laminae in the silicilyte; each lamination would represent the remnant of a microbial mat that fell to the seafloor covered in silica. It is important to note, as discussed above (Section 4.1), that the presence of laminae neither requires nor demonstrates the presence of microbial mats. Before the advent of significant bioturbation in the Cambrian, laminated rocks derived from chemical sediments were ubiquitous (Grotzinger & James, 2000). Such laminated rocks can form through purely abiotic means via the settling of particles from the water column (Grotzinger & Knoll, 1999; Grotzinger & Rawahi, 2014; Grotzinger & Rothman, 1996). Although the presence of microbial mats is probable in such environments, their importance in creating laminae requires the identification of specific textures such as trapping and binding textures, crinkly laminae, or even low-relief stromatolites. None of these are found in the silicilyte. Thus, although microbial mats may be responsible for the laminae as argued by Al Rajaibi et al. (2015) and Amthor et al. (2005), there is no direct evidence for this mechanism, nor is it necessary.

5.2 | Coupled chemical and physical model for the formation of the Athel silicilyte

We propose a model for the Athel Basin in which biologically productive surface waters generated organic matter that, via templating, caused silica nucleation (Figure 13). These silica-coated organic

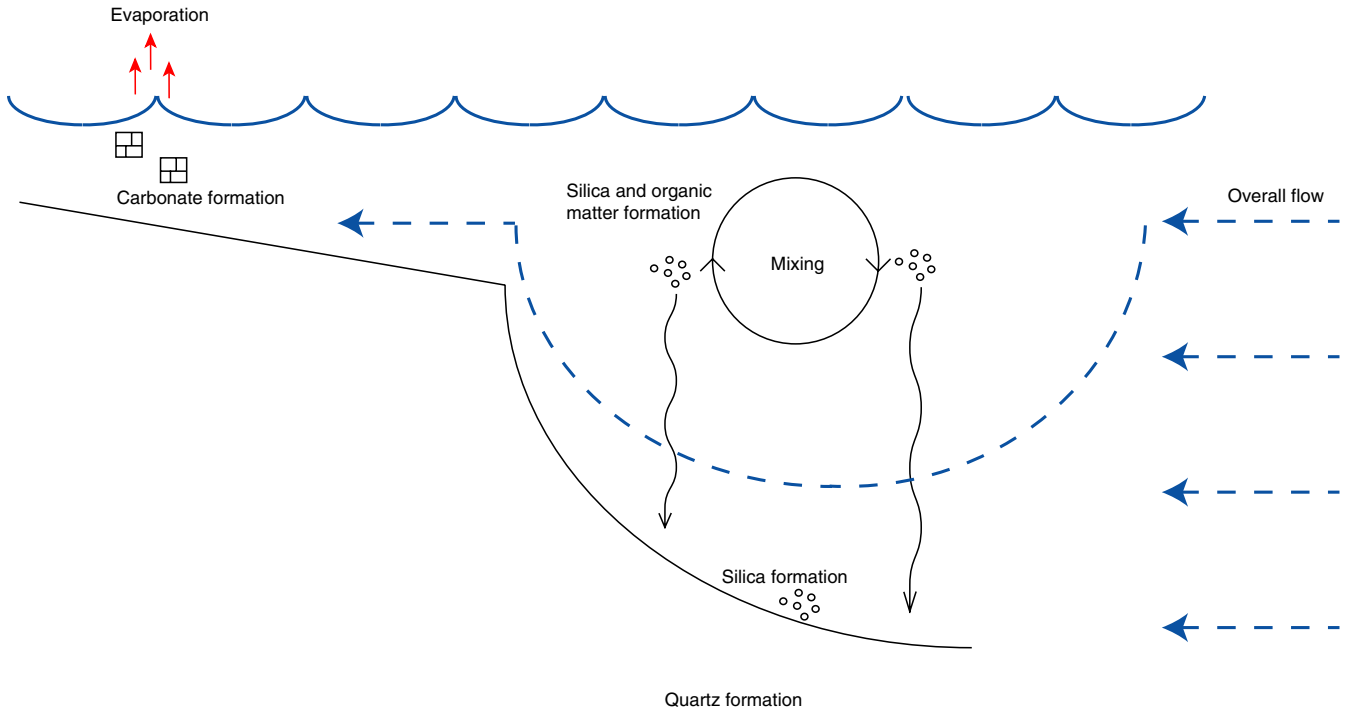

FIGURE 13 Schematic representation for silica and organic matter formation in the Athel Basin. We propose a model where water flows into the basin and mixes vertically above the site of silica deposition. Silica nucleates via templation on newly formed organic matter and then sinks to the seafloor, forming the silicilyte. The organic matter is then respired at depth (leaving behind a silica-enriched residue) and the nutrients returned to the surface via mixing, fueling further production and silica nucleation. Silica precipitation on organic matter would remove silica from the system before shoaling on the Ara platform preventing silica oversaturation during evaporation and carbonate growth

particles would have been sufficiently dense to settle to the seafloor and thus create the silica-enriched sediment that later became the silicilyte. As the silicilyte is enriched in silica compared to organic matter (~85:1 by weight), the model requires that most of the original organic matter was remineralized at depth either in the sediments or bottom waters. This remineralization would release nutrients (e.g., phosphate) back to the water column, which, when mixed back with surface waters, would allow for continued primary production in the photic zone.

This model is consistent with many of the observations made from the petrographic, organic, and inorganic measurements: To first order, the model ensures silica delivery to the Athel Basin sediments and would lower silica levels in the water column such that silica could not precipitate on the adjacent carbonate shelf. Additionally, because primary production rates, which control silica fluxes to the sediment, commonly vary seasonally, silica fluxes would be expected to vary too creating a mechanism to generate laminae.

The organic matter delivered to the sediment/water interface would stimulate respiration removing oxygen (if present) or converting sulfate to sulfide. The loss of O_2 and increased reduction of sulfate to sulfide is captured by the increase in biomarkers related to reducing conditions in silicilyte biomarkers and elevated Fe_{Py}/Fe_{HR} in the sediments. Importantly, we note that the organic biomarker ratios that are sensitive to redox/stratification conditions *do not* differentiate between sedimentary and bottom water conditions. Thus, the biomarkers only necessitate increasingly reduced conditions in the sediments.

Mixing of deep, nutrient-rich waters with surface waters in the Athel Basin would also have influenced the photosynthetic communities present. Differences in the photosynthetic communities are consistent with the changes in the 2-MHI, $\%C_{29}$ biomarker parameters, and sterane:hopane ratios in the silicilyte vs. the shales. The increase in 2-MHI and $\%C_{29}$ values in silicilyte relative to the shale samples can be interpreted to indicate increases in the relative importance of cyanobacteria to all bacteria (although alternative explanations are also possible as discussed above). The higher $\%C_{29}$ values in the silicilyte relative to the shale samples indicates an increase in the contribution of green algae to preserved algal biomass. Finally, the lower sterane/hopane ratio in the silicilyte vs. the bounding shales suggests a subtle increase in bacteria relative to eukaryotic biomass in water column.

Our proposed model of the environmental conditions during silicilyte deposition in which deeper, O_2-depleted, and nutrient-rich waters mixed with surface waters can explain these biomarker shifts. In modern systems, upwelled low O_2 waters often have experienced loss of nitrate via denitrification either in the water column or sediments. As a result, organisms that can fix nitrogen or are adapted to using ammonia as their nitrogen source instead of nitrate have an advantage in such environments. Indeed, in the modern ocean, upwelled denitrified waters are areas of intense nitrogen fixation (Deutsch, Sarmiento, Sigman, Gruber, & Dunne, 2007). As cyanobacteria are the major nitrogen fixers in the oceans today (Zehr, 2011), the increase in the 2-methylhopane index (possibly indicating increased cyanobacterial contributions to bacterial

biomass) and the lower sterane/hopane ratios during silicilyte deposition is consistent with our model. Finally, green algae have a stronger preference for ammonia over nitrate as compared to other algae. Thus, green algae could fare better in nitrate limited environments (Litchman, Klausmeier, Schofield, & Falkowski, 2007). This is consistent with the increased $\%C_{29}$ sterane values in the silicilyte vs. the bounding shales.

Finally, the MMAs indicate that an unknown organism, or group of organisms contributed significantly (~10s of percent) to the total mass of preserved organic matter during the deposition of the silicilyte. As discussed above (Section 4.2.2), no known organisms have been found that produce the precursors of the MMAs found in the silicilyte. However, Love et al. (2008) hypothesized that sulfide-oxidizing organisms living at the chemocline in microbial mats may have been the source of these alkanes. If correct, such organisms could have occupied the sediment–water interface and may have thrived during silicilyte deposition due to lower siliciclastic depositional rates (see below)—generally high siliciclastic inputs prevent the establishment of microbial mats. As discussed in Lee et al. (2013), such elevated MMA values could indicate substantial contributions of benthic biomass to the preserved organic matter.

A question is why the shales, which also have similar biomarker ratios and iron speciation values, did not also develop into silicilytes. An explanation is that during shale deposition, terrigenous inputs overwhelmed the lower, background silica fluxes. The silicilyte would thus represent a sediment-starved, condensed geological section. Furthermore, sorption of organic carbon onto the high surface-area clay minerals (Hedges & Keil, 1995; Mayer, 1994) could have removed organic carbon from the water column, thus lowering the concentrations of substrates promoting silica nucleation. Sorption and protection of organic matter on clay minerals (Hedges & Keil, 1995; Mayer, 1994) could also explain the relative enrichment of organic carbon in the shales vs. the silicilyte.

Importantly, this model implicitly requires that silicilyte-like environments did not only exist during the A4 cycle (Figure 2), but also existed throughout the entire deposition of the Ara carbonates. This is because no Ara carbonates contain significant concentrations of authigenic quartz. Thus, the presence of older or younger silicilytes during Ara time, or in systems outside of the Athel Basin would provide additional evidence for this model. Preliminary data from two silica-rich deposits (66 and 77% by weight SiO_2) in Oman from a well correlated to the A3 carbonate may indicate other silicilyte-like environments. These samples contain MMAs, which are found in abundance in the silicilyte. However, we note that MMAs are not unique to the silicilyte and are found elsewhere in high abundances in the South Oman Salt Basin (Lee et al., 2013). Additional interrogation of this core is necessary, but opens the possibility for other silicilytes in Oman.

6 | 24-IPC/NPC RATIOS AND ATHEL BASIN WATER COLUMN CHEMISTRY

The biomarker ratios measured that are sensitive to redox conditions (the bisnorhopane, homohopane, and gammacerane indices) all indicate that anoxic/stratified conditions became more intense in the sediments and potentially at the sediment–water interface or in the water column during silicilyte deposition as compared to shale deposition. The iron speciation data are consistent with sulfide accumulation in the sediments and potentially intermittently in the water column during both shale and silicilyte deposition. Concurrent to the change in the redox-sensitive biomarker ratios, 24-ipc/npc ratios rose during silicilyte deposition relative to the shales. Interestingly, the only known organisms that synthesize significant quantities of 24-ipc precursors are adult demosponges (see Love & Summons, 2015 for a compelte discussion), which are benthic, obligate aerobes. At first blush, increasingly reducing conditions at depth would appear inconsistent with an environment that favors obligately aerobic eukaryotes. We explore two explanations for the concurrent changes in the biomarker and iron speciation ratios.

In the first explanation, we allow that the 24-ipc precursors were produced by adult sponges living at the sediment–water interface. This hypothesis has strong merit as adult sponges are the only known organisms that synthesize sufficient quantities of 24-ipc precursors to create elevated (>0.5) 24-ipc/npc ratios (Love & Summons, 2015; Love et al., 2009). Furthermore, algae that make trace amounts of 24-ipc precursors today appear not to have acquired this capacity until the Phanerozoic (Gold, Grabenstatter, et al., 2016). This explanation additionally follows the interpretative frameworks put forward by previous studies (e.g., Gold, Grabenstatter, et al., 2016; Grosjean et al., 2009; Love & Summons, 2015; Love et al., 2009; McCaffrey et al., 1994). Importantly, this scenario requires that sponges proliferated in an increasingly O_2-deficient environment during silicilyte deposition. We note, though, that episodic mixing of deep and shallow waters, as we proposed occurred during silicilyte formation (see Section 5), could have allowed for times of increased oxygenation at the sediment–water interface. Additionally, it is important to stress that the redox-sensitive biomarkers and iron speciation data only require shifts in sedimentary conditions. Thus, the presence of low (and perhaps episodic) but finite concentrations of O_2 in deep waters of the Athel basin is consistent with these other measures of the redox conditions in the Athel Basin.

The redox-sensitive biomarkers do indicate that O_2 levels were likely lower at the sediment–water interface (given an increase in reducing conditions in the sediment). Thus, a key question is whether sponges living at low dissolved O_2 concentrations is reasonable to propose? Theoretical and experimental studies show that sponges can survive at around ~1% of present atmospheric oxygen levels (Mills et al., 2014; Sperling, Halverson, Knoll, Macdonald, & Johnston, 2013). Additionally, sponge interiors can become anoxic (Hoffmann et al., 2005), sponges harbor obligate anaerobic symbionts (Hoffmann et al., 2005; Webster, Wilson, Blackall, & Hill, 2001), and sponges can survive episodes of anoxia (Bell & Barnes, 2000; Mills et al., 2014). Thus, the presence of sponge biomarkers in a system poised at the boundary between anoxic and oxic conditions is perhaps not actually surprising.

An alternative explanation for the increase in 24-ipc/npc ratios during silicilyte deposition along with the apparent increase in reducing conditions at depth is that 24-ipc precursors were not generated by adult demosponges. For example, in addition to adult sponges,

other potential sources for Neoproterozoic 24-ipc have also been discussed and include sponge larvae (some of which are pelagic) or pelagic ancestors to sponges such as stem-group sponges or stem-group animals (e.g., Brocks & Butterfield, 2009; Lee et al., 2013). We note that modern sponge larvae today generally only live for hours to days, swim at speeds of ~1 km/day (Maldonado & Bergquist, 2002), and are rarely observed in offshore plankton populations (Maldonado, 2006). Thus, we consider the large-scale transport of larvae from outside of the Athel Basin to its interior to be unlikely.

Alternative sources for the 24-ipc precursors in Neoproterozoic–Cambrian Oman rocks that have been considered include pelagic spongal ancestors (e.g., stem-group sponges or stem-group animals; Brocks & Butterfield, 2009; Lee et al., 2013). Such scenarios are appealing as they would allow the biomarker and iron speciation data to be interpreted in a straightforward manner; that is, that the water column was generally anoxic below the mixed layer as previous studies have argued (Al Rajaibi et al., 2015; Amthor et al., 2005; Ramseyer et al., 2013; Schröder & Grotzinger, 2007; Wille et al., 2008). Additionally, if such organisms did not generate spicules, this could explain the lack of fossil spicules in Neoproterozoic Oman rocks despite elevated (>0.5) 24-ipc/npc ratios—it should be noted, though, that not all adult demosponges produce spicules. Such a scenario is independently supported by the hypothesis that stem-group sponges were pelagic (Nielsen, 2008). Although genetic analyses of the enzymes involved in the synthesis of 24-ipc precursors in sponges is consistent with sponges being the source of these biomarkers in the Neoproterozoic (Gold, Grabenstatter, et al., 2016), such analyses are also consistent with 24-ipc being generated by stem-group sponges or stem-group animals (Gold, O'reilly, Luo, Briggs, & Summons, 2016). Finally, we note that elevated abundances of 24-ipc and 24-ipc/npc ratios >0.5 are found in numerous Neoproterozoic, Cambrian, and Ordovician oils and bitumens (McCaffrey et al., 1994; Peters et al., 2005). If stem-group sponges or animals were responsible for the Neoproterozoic 24-ipc biomarkers, then they either would have had to have persisted ~100 million years into the Phanerozoic or been replaced by sponges as the source of the 24-ipc in the Phanerozoic.

Regardless of whether the 24-ipc precursors were generated by crown-group, adult, benthic sponges or ancestor to sponges (and therefore animals), the silicilyte appears to have been a site of preferential 24-ipc precursor generation. Consequently, water columns similar to the Athel Basin during silicilyte generation, that is, deep-water settings with high-productivity water columns, may have been the sorts of environments where early animals proliferated.

7 | THE CONNECTION BETWEEN THE SILICILYTE AND GLOBAL BIOGEOCHEMICAL CONDITIONS

Although no other *bona fide* silicilytes exist in the geologic record, Brasier, Antcliffe, and Callow (2011) noted an increase in subtidal silicification at the Ediacaran–Cambrian boundary. This expansion is evidenced by the laminated cherts in the Tal Formation in India (Brasier et al., 2011), which have been interpreted to have formed in a subtidal setting (Mazumdar & Banerjee, 1998) and in the Yangtze platform in China (Shen & Schidlowski, 2000). Brasier et al. (2011) suggested that these systems (including the silicilyte) were all sites of elevated primary production.

These other formations are not exact analogues to the silicilyte. For example, the Tal Formation cherts are associated with phosphorite deposits (Mazumdar & Banerjee, 1998) while some (but not all) Yangtze platform cherts may have had a local hydrothermal source (Wang et al., 2012). Regardless, the presence of other productive, deep-water silica deposits formed close to the time of the silicilyte could indicate that the silicilyte is an expression of a more global phenomenon occurring at the Ediacaran–Cambrian boundary. One possibility for such an expansion, as proposed by Ramseyer et al. (2013), is elevated silica fluxes to the oceans due to increased silicate weathering rates.

Consequently, before the expansion of sponges and radiolaria in the Cambrian, which fundamentally altered the location of silica deposition (Maliva, Knoll, & Siever, 1989), deep-water silica deposition in productive waters may have been an important sink of silica to the solid Earth. The silicilyte would represent an end member of these systems where low siliciclastic inputs allowed for the full expression of a silica-dominated depositional environment. This predicts that silicilyte-like formations could be present in other deep-water, sediment-starved basins at the time of the Ediacaran–Cambrian boundary and perhaps even earlier in the Proterozoic.

8 | SUMMARY AND CONCLUSIONS

The silicilyte is an enigmatic rock type, is singular in the rock record, has no known modern analogues, and appears only at the Ediacaran–Cambrian boundary. Previous studies proposed that its original depositional environment was a permanently anoxic, sulfidic water column. Silica precipitation occurred due to either nucleation on floating microbial mats or due to mixing of surface and deep waters with significantly different salinities (Al Rajaibi et al., 2015; Amthor et al., 2005; Ramseyer et al., 2013; Schröder & Grotzinger, 2007; Wille et al., 2010).

Our biomarker results indicate that the silicilyte received organic matter from a distinct assemblage of biological sources as compared to the bounding shales. This indicates that: (i) The silicilyte was more reducing at depth in the water column or in its sediment pore waters than the bounding Thuleilat Shale and U-Shale. (ii) The silicilyte relative to the bounding shales received a higher input of organic matter sourced from bacteria vs. eukaryotes, from green algae vs. other eukaryotes, and from bacteria like cyanobacteria or Proteobacteria that synthesize 2-methylhopane precursors vs. other bacteria. (iii) High monomethylalkane abundances potentially suggest a significant input of organic matter to the ultimately preserved hydrocarbons in the silicilyte from benthic microbial mats. And (iv), based on measurements of 24 iso/*n*-propylcholestane ratios (and total abundances of 24-isopropylcholestane vs. total organic carbon), the silicilyte received

an increase in biomass from sponges or ancestors to sponges/animals to the preserved organic carbon relative to the bounding shales.

Iron speciation data indicate that sulfide was produced in the system (as evidenced by the presence of pyrite). However, the amount of pyrite relative to other phases of iron susceptible to pyritization is lower than that commonly observed in permanently euxinic water bodies. This difference indicates that the Athel waters were not permanently sulfidic and likely experienced episodic ventilation with oxygenated seawater and thus redox variability in bottom waters.

Based on both the new observations presented here as well as those made in previous studies, we propose that the silicilyte formed via silica precipitation on organic matter formed in the upper water column of the Athel Basin during mixing of nutrient-rich deeper waters with ocean waters entering the basin. This silica then settled to the seafloor and formed the sedimentary precursors of silicilyte. Organic matter was remineralized at depth creating the silica enrichments observed in the silicilyte. Silicon isotope measurements of the quartz do not indicate that spongal opal was the precursor to quartz silicilyte. The oxygen isotopes of quartz in the silicilyte show that the silica transformed to quartz during diagenesis over multiple kilometers of depth in the sedimentary column under evolving temperatures and or/pore-water compositions.

The silicilyte, although unique in the record, appears to have analogs in other basins of Ediacaran–Cambrian boundary age. These other systems accumulated silica in deeper water and are also thought to have been productive environments. This similarity may indicate that the silicilyte is a sediment-starved end member of a form of silica deposition that occurred at this time. It may represent an underappreciated form of silica removal from the oceans in the Proterozoic.

ACKNOWLEDGMENTS

We acknowledge funding from the Eaton Fellowship administered by the Division of Geological and Planetary Sciences at Caltech and the NSF GRFP. Petroleum Development Oman is thanked for project planning assistance, sample access, and stimulating scientific discussions. We acknowledge the Ministry of Oil and Gas of the Sultanate of Oman for permission to access samples and to publish the results. We thank three anonymous reviewers and our handling editor, Jochen Brocks, for helpful comments that greatly improved the manuscript.

CONFLICT OF INTEREST

All authors declare no conflict of interest.

REFERENCES

Al Rajaibi, I. M., Hollis, C., & Macquaker, J. H. (2015). Origin and variability of a terminal Proterozoic primary silica precipitate, Athel Silicilyte, South Oman Salt Basin, Sultanate of Oman. *Sedimentology*, *62*, 793–825.

Allen, P. A. (2007). The Huqf supergroup of Oman: Basin development and context for Neoproterozoic glaciation. *Earth-Science Reviews*, *84*, 139–185.

Amthor, J. E., Grotzinger, J. P., Schröder, S., Bowring, S. A., Ramezani, J., Martin, M. W., & Matter, A. (2003). Extinction of cloudina and namacalathus at the precambrian-cambrian boundary in oman. *Geology*, *31*, 431–434.

Amthor, J. E., Ramseyer, K., Faulkner, T., & Lucas, P. (2005). Stratigraphy and sedimentology of a chert reservoir at the Precambrian-cambrian boundary: The Al Shomou Silicilyte, South Oman Salt Basin. *GeoArabia*, *10*, 89–122.

Antcliffe, J. B. (2013). Questioning the evidence of organic compounds called sponge biomarkers. *Palaeontology*, *56*, 917–925.

Antcliffe, J. B., Callow, R. H., & Brasier, M. D. (2014). Giving the early fossil record of sponges a squeeze. *Biological Reviews*, *89*, 972–1004.

Bailey, J. V., Joye, S. B., Kalanetra, K. M., Flood, B. E., & Corsetti, F. A. (2007). Evidence of giant sulphur bacteria in Neoproterozoic phosphorites. *Nature*, *445*, 198–201.

Bazhenova, O. K., & Arefiev, O. A. (1996). Geochemical peculiarities of Pre-Cambrian source rocks in the East European Platform. *Organic Geochemistry*, *25*, 341–351.

Bell, J. J., & Barnes, D. K. A. (2000). A sponge diversity centre within a marine 'island'. *Hydrobiologia*, *440*, 55–64.

Bishop, A. N., & Farrimond, P. (1995). A new method of comparing extended hopane distributions. *Organic Geochemistry*, *23*, 987–990.

Blatt, H. (1987). Oxygen isotopes and the origin of quartz. *Journal of Sedimentary Research*, *57*, 373–377.

Bowring, S. A., Grotzinger, J. P., Condon, D. J., Ramezani, J., Newall, M. J., & Allen, P. A. (2007). Geochronologic constraints on the chronostratigraphic framework of the Neoproterozoic Huqf Supergroup, Sultanate of Oman. *American Journal of Science*, *307*, 1097–1145.

Brasier, M. D., Antcliffe, J. B., & Callow, R. H. T. (2011). Evolutionary trends in remarkable fossil preservation across the Ediacaran–Cambrian transition and the impact of metazoan mixing. In D. J. Bottjer & P. A. Allison (Eds.), *Taphonomy: Process and bias through time* (519–567). Dordrecht: Springer.

Brasier, M. D., Green, O., & Shields, G. (1997). Ediacarian sponge spicule clusters from southwestern Mongolia and the origins of the Cambrian fauna. *Geology*, *25*, 303–306.

Brocks, J. J., & Butterfield, N. J. (2009). Biogeochemistry: Early animals out in the cold. *Nature*, *457*, 672–673.

Brocks, J. J., Logan, G. A., Buick, R., & Summons, R. E. (1999). Archean molecular fossils and the early rise of eukaryotes. *Science*, *285*, 1033–1036.

Brocks, J., & Summons, R. (2005). Biomarkers for early life. *Biogeochemistry*, *8*, 63.

Butterfield, N. (2009). Oxygen, animals and oceanic ventilation: An alternative view. *Geobiology*, *7*, 1–7.

Canfield, D. E., Poulton, S. W., Knoll, A. H., Narbonne, G. M., Ross, G., Goldberg, T., & Strauss, H. (2008). Ferruginous conditions dominated later Neoproterozoic deep-water chemistry. *Science*, *321*, 949–952.

Canfield, D. E., Raiswell, R., & Bottrell, S. (1992). The reactivity of sedimentary iron minerals toward sulfide. *American Journal of Science*, *292*, 659–683.

Cao, C., Love, G. D., Hays, L. E., Wang, W., Shen, S., & Summons, R. E. (2009). Biogeochemical evidence for euxinic oceans and ecological disturbance presaging the end-Permian mass extinction event. *Earth and Planetary Science Letters*, *281*, 188–201.

Clarkson, M., Poulton, S., Guilbaud, R., & Wood, R. (2014). Assessing the utility of Fe/Al and Fe-speciation to record water column redox conditions in carbonate-rich sediments. *Chemical Geology*, *382*, 111–122.

Cohen, P. A., Knoll, A. H., & Kodner, R. B. (2009). Large spinose microfossils in Ediacaran rocks as resting stages of early animals. *PNAS*, *106*, 6519–6524.

Davidson, E. H., & Erwin, D. H. (2009). An integrated view of Precambrian eumetazoan evolution. *Cold Spring Harbor Symposia on Quantitative Biology*, *74*, 65–80.

Deutsch, C., Sarmiento, J. L., Sigman, D. M., Gruber, N., & Dunne, J. P. (2007). Spatial coupling of nitrogen inputs and losses in the ocean. *Nature*, *445*, 163–167.

Douthitt, C. (1982). The geochemistry of the stable isotopes of silicon. *Geochimica et Cosmochimica Acta*, *46*, 1449–1458.

Droser, M. L., & Gehling, J. G. (2015). The advent of animals: The view from the Ediacaran. *PNAS*, *112*, 4865–4870.

Fedonkin, M. A., & Waggoner, B. M. (1997). The late Precambrian fossil Kimberella is a mollusc-like bilaterian organism. *Nature*, *388*, 868–870.

Fein, J. B., Scott, S., & Rivera, N. (2002). The effect of Fe on Si adsorption by *Bacillus subtilis* cell walls: Insights into non-metabolic bacterial precipitation of silicate minerals. *Chemical Geology*, *182*, 265–273.

Ferris, F. G., Fyfe, W. S., & Beveridge, T. J. (1988). Metallic ion binding by *Bacillus subtilis*: Implications for the fossilization of microorganisms. *Geology*, *16*, 149–152.

Fowler, M., & Douglas, A. (1987). Saturated hydrocarbon biomarkers in oils of Late Precambrian age from Eastern Siberia. *Organic Geochemistry*, *11*, 201–213.

Gold, D. A., Grabenstatter, J., De Mendoza, A., Riesgo, A., Ruiz-Trillo, I., & Summons, R. E. (2016). Sterol and genomic analyses validate the sponge biomarker hypothesis. *PNAS*, *113*, 2684–2689.

Gold, D. A., O'reilly, S. S., Luo, G., Briggs, D. E., & Summons, R. E. (2016). Prospects for sterane preservation in sponge fossils from museum collections and the utility of sponge biomarkers for molecular clocks. *Bulletin of the Peabody Museum of Natural History*, *57*, 181–189.

Grantham, P. (1988). Origin of crude oils in Oman. *Journal of Petroleum Geology*, *11*, 61–80.

Grosjean, E., Love, G., Stalvies, C., Fike, D., & Summons, R. (2009). Origin of petroleum in the Neoproterozoic-Cambrian South Oman Salt Basin. *Organic Geochemistry*, *40*, 87–110.

Grotzinger, J. P., & James, N. P. (2000). Precambrian carbonates: evolution of understanding In J. P. Grotzinger & N. P. James (Eds.), *Carbonate sedimentation and diagenesis in the evolving precambrian world* (pp. 3–20). Tulsa, OK: SEPM Special Publication.

Grotzinger, J. P., & Knoll, A. H. (1999). Stromatolites in Precambrian carbonates: Evolutionary mileposts or environmental dipsticks? *Annual Review of Earth and Planetary Sciences*, *27*, 313–358.

Grotzinger, J., & Rawahi, Z. (2014). Depositional facies and platform architecture of microbialite-dominated carbonate reservoirs, Ediacaran-Cambrian Ara Group, Sultanate of Oman. *AAPG Bulletin*, *98*, 1453–1494.

Grotzinger, J. P., & Rothman, D. H. (1996). An abiotic model for stromatolite morphogenesis. *Nature*, *383*, 423–425.

Haven, H. L. T., Rohmer, M., Rullkötter, J., & Bisseret, P. (1989). Tetrahymanol, the most likely precursor of gammacerane, occurs ubiquitously in marine sediments. *Geochimica et Cosmochimica Acta*, *53*, 3073–3079.

Hedges, J. I., & Keil, R. G. (1995). Sedimentary organic matter preservation: An assessment and speculative synthesis. *Marine Chemistry*, *49*, 81–115.

Hendry, K. R., & Robinson, L. F. (2012). The relationship between silicon isotope fractionation in sponges and silicic acid concentration: Modern and core-top studies of biogenic opal. *Geochimica et Cosmochimica Acta*, *81*, 1–12.

Hoffman, P. F., Kaufman, A. J., Halverson, G. P., & Schrag, D. P. (1998). A Neoproterozoic snowball earth. *Science*, *281*, 1342–1346.

Hoffmann, F., Larsen, O., Thiel, V., Rapp, H. T., Pape, T., Michaelis, W., & Reitner, J. (2005). An anaerobic world in sponges. *Geomicrobiology Journal*, *22*, 1–10.

Höld, I. M., Schouten, S., Jellema, J., & Sinninghe Damsté, J. S. (1999). Origin of free and bound mid-chain methyl alkanes in oils, bitumens and kerogens of the marine, Infracambrian Huqf Formation (Oman). *Organic Geochemistry*, *30*, 1411–1428.

Jiamo, F., Guoying, S., Pingan, P., Brassell, S. C., Eglinton, G., & Jigang, J. (1986). Peculiarities of salt lake sediments as potential source rocks in China. *Organic Geochemistry*, *10*, 119–126.

Kelly, A. E., Love, G. D., Zumberge, J. E., & Summons, R. E. (2012). Hydrocarbon biomarkers of Neoproterozoic to Lower Cambrian oils from eastern Siberia. *Organic Geochemistry*, *42*, 640–654.

Kenig, F., Damsté, J. S. S., Kock-Van Dalen, A., Rijpstra, W. I. C., Huc, A. Y., & De Leeuw, J. W. (1995). Occurrence and origin of mono-, di-, and trimethylalkanes in modern and Holocene cyanobacterial mats from Abu Dhabi, United Arab Emirates. *Geochimica et Cosmochimica Acta*, *59*, 2999–3015.

Kirschvink, J. L., & Raub, T. D. (2003). A methane fuse for the Cambrian explosion: Carbon cycles and true polar wander. *Comptes Rendus Geoscience*, *335*, 65–78.

Kleemann, G., Poralla, K., Englert, G., Kjøsen, H., Liaaen-Jensen, S. V., Neunlist, S., & Rohmer, M. (1990). Tetrahymanol from the phototrophic bacterium Rhodopseudomonas palustris: First report of a gammacerane triterpene from a prokaryote. *Journal of General Microbiology*, *136*, 2551–2553.

Klomp, U. C. (1986). The chemical structure of a pronounced series of isoalkanes in South Oman crudes. *Organic Geochemistry*, *10*, 807–814.

Knauth, L. P., & Epstein, S. (1976). Hydrogen and oxygen isotope ratios in nodular and bedded cherts. *Geochimica et Cosmochimica Acta*, *40*, 1095–1108.

Knoll, A. H. (1985). Exceptional preservation of photosynthetic organisms in silicified carbonates and silicified peats. *Philosophical Transactions of the Royal Society of London B, Biological Sciences*, *311*, 111–122.

Knoll, A. H., & Golubic, S. (1979). Anatomy and taphonomy of a Precambrian algal stromatolite. *Precambrian Research*, *10*, 115–151.

Kodner, R. B., Summons, R. E., Pearson, A., King, N., & Knoll, A. H. (2008). Sterols in a unicellular relative of the metazoans. *PNAS*, *105*, 9897–9902.

Konhauser, K. O., Jones, B., Phoenix, V. R., Ferris, G., & Renaut, R. W. (2004). The microbial role in hot spring silicification. *AMBIO: A Journal of the Human Environment*, *33*, 552–558.

Lafargue, E., Marquis, F., & Pillot, D. (1998). Rock-Eval 6 applications in hydrocarbon exploration, production, and soil contamination studies. *Oil & Gas Science and Technology – Revue de L'Institut Français du Pétrole*, *53*, 421–437.

Lee, C., Fike, D., Love, G., Sessions, A., Grotzinger, J., Summons, R., & Fischer, W. (2013). Carbon isotopes and lipid biomarkers from organic-rich facies of the Shuram Formation, Sultanate of Oman. *Geobiology*, *11*, 406–419.

Leo, R. F., & Barghoorn, E. S. (1976). Silicification of wood. *Botanical Museum Leaflets, Harvard University*, *25*, 1–47.

Li, C. W., Chen, J. Y., & Hua, T. E. (1998). Precambrian sponges with cellular structures. *Science*, *279*, 879.

Litchman, E., Klausmeier, C. A., Schofield, O. M., & Falkowski, P. G. (2007). The role of functional traits and trade-offs in structuring phytoplankton communities: Scaling from cellular to ecosystem level. *Ecology Letters*, *10*, 1170–1181.

Love, G. D., Grosjean, E., Stalvies, C., Fike, D. A., Grotzinger, J. P., Bradley, A. S., … Summons, R. E. (2009). Fossil steroids record the appearance of Demospongiae during the Cryogenian period. *Nature*, *457*, 718–721.

Love, G. D., Snape, C. E., Carr, A. D., & Houghton, R. C. (1995). Release of covalently-bound alkane biomarkers in high yields from kerogen via catalytic hydropyrolysis. *Organic Geochemistry*, *23*, 981–986.

Love, G. D., Stalvies, C., Grosjean, E., Meredith, W., & Snape, C. E. (2008). Analysis of molecular biomarkers covalently bound within Neoproterozoic sedimentary kerogen. *Paleontological Society Papers*, *14*, 67–83.

Love, G. D., & Summons, R. E. (2015). The molecular record of Cryogenian sponges–a response to Antcliffe (2013). *Palaeontology*, *58*(6), 1131–1136.

Lyons, T. W., & Severmann, S. (2006). A critical look at iron paleoredox proxies: New insights from modern euxinic marine basins. *Geochimica et Cosmochimica Acta*, *70*, 5698–5722.

Maldonado, M. (2006). The ecology of the sponge larva. *Canadian Journal of Zoology*, *84*, 175–194.

Maldonado, M., & Bergquist, P. R. (2002). Phylum Porifera. In C. M. Young & M. A. Sewell (Eds.), *Atlas of marine invertebrate larvae* (pp. 21–50). San Diego: Academic Press.

Maliva, R. G., Knoll, A. H., & Siever, R. (1989). Secular change in chert distribution: A reflection of evolving biological participation in the silica cycle. *Palaios*, *4*, 519–532.

Maliva, R. G., Knoll, A. H., & Simonson, B. M. (2005). Secular change in the Precambrian silica cycle: Insights from chert petrology. *Geological Society of America Bulletin*, *117*, 835–845.

Maloof, A. C., Rose, C. V., Beach, R., Samuels, B. M., Calmet, C. C., Erwin, D. H., … Simons, F. J. (2010). Possible animal-body fossils in pre-Marinoan limestones from South Australia. *Nature Geoscience*, *3*, 653–659.

Marin-Carbonne, J., Chaussidon, M., & Robert, F. (2010). Microscale oxygen isotope variations in 1.9 Ga Gunflint cherts: Assessments of diagenesis effects and implications for oceanic paleotemperature reconstructions. *Geochimica et Cosmochimica Acta*, *74*, 116–130.

Marshall, C. R. (2006). Explaining the Cambrian "explosion" of animals. *Annual Review of Earth and Planetary Sciences*, *34*, 355–384.

Mayer, L. M. (1994). Surface area control of organic carbon accumulation in continental shelf sediments. *Geochimica et Cosmochimica Acta*, *58*, 1271–1284.

Mazumdar, A., & Banerjee, D. (1998). Siliceous sponge spicules in the Early Cambrian chert-phosphorite member of the Lower Tal Formation, Krol belt, Lesser Himalaya. *Geology*, *26*, 899–902.

McCaffrey, M. A., Michael Moldowan, J., Lipton, P. A., Summons, R. E., Peters, K. E., Jeganathan, A., & Watt, D. S. (1994). Paleoenvironmental implications of novel C_{30} steranes in Precambrian to Cenozoic age petroleum and bitumen. *Geochimica et Cosmochimica Acta*, *58*, 529–532.

Mills, D. B., & Canfield, D. E. (2014). Oxygen and animal evolution: did a rise of atmospheric oxygen "trigger" the origin of animals? *BioEssays*, *36*, 1145–1155.

Mills, D. B., Ward, L. M., Jones, C., Sweeten, B., Forth, M., Treusch, A. H., & Canfield, D. E. (2014). Oxygen requirements of the earliest animals. *Proceedings of the National Academy of Sciences*, *111*(11), 4168–4172.

Moldowan, J. M., Fago, F. J., Lee, C. Y., Jacobson, S. R., Watt, D. S., Slougui, N.-E., … Young, D. C. (1990). Sedimentary 12-n-Propylcholestanes, molecular fossils diagnostic of marine algae. *Science*, *247*, 309–312.

Moldowan, J. M., Seifert, W. K., & Gallegos, E. J. (1985). Relationship between petroleum composition and depositional environment of petroleum source rocks. *AAPG Bulletin*, *69*, 1255–1268.

Mountain, B. W., Benning, L. G., & Boerema, J. A. (2003). Experimental studies on New Zealand hot spring sinters: Rates of growth and textural development. *Canadian Journal of Earth Sciences*, *40*, 1643–1667.

Nielsen, C. (2008). Six major steps in animal evolution: Are we derived sponge larvae? *Evolution & Development*, *10*, 241–257.

Pawlowska, M. M., Butterfield, N. J., & Brocks, J. J. (2013). Lipid taphonomy in the Proterozoic and the effect of microbial mats on biomarker preservation. *Geology*, *41*, 103–106.

Peters, K. E. (1986). Guidelines for evaluating petroleum source rock using programmed pyrolysis. *AAPG Bulletin*, *70*, 318–329.

Peters, K. E., Clark, M. E., Gupta, U. D., McCaffrey, M. A., & Lee, C. Y. (1995). Recognition of an Infracambrian source rock based on biomarkers in the Baghewala-1 oil, India. *AAPG Bulletin*, *79*, 1481–1493.

Peters, K. E., Walters, C., & Moldowan, J. (2005). *The biomarker guide: Volume II. Biomarkers and isotopes in petroleum systems and earth history*. Cambridge, UK: Cambridge University Press.

Planavsky, N. J., Mcgoldrick, P., Scott, C. T., Li, C., Reinhard, C. T., Kelly, A. E., … Lyons, T. W. (2011). Widespread iron-rich conditions in the mid-Proterozoic ocean. *Nature*, *477*, 448–451.

Poulton, S. W., & Canfield, D. E. (2005). Development of a sequential extraction procedure for iron: Implications for iron partitioning in continentally derived particulates. *Chemical Geology*, *214*, 209–221.

Poulton, S. W., & Canfield, D. E. (2011). Ferruginous conditions: A dominant feature of the ocean through Earth's history. *Elements*, *7*, 107–112.

Raiswell, R., Buckley, F., Berner, R. A., & Anderson, T. (1988). Degree of pyritization of iron as a paleoenvironmental indicator of bottom-water oxygenation. *Journal of Sedimentary Research*, *58*, 812–819.

Raiswell, R., & Canfield, D. E. (1998). Sources of iron for pyrite formation in marine sediments. *American Journal of Science*, *298*, 219–245.

Ramseyer, K., Amthor, J. E., Matter, A., Pettke, T., Wille, M., & Fallick, A. E. (2013). Primary silica precipitate at the Precambrian/Cambrian boundary in the South Oman Salt Basin, Sultanate of Oman. *Marine and Petroleum Geology*, *39*(1), 187–197.

Rashby, S. E., Sessions, A. L., Summons, R. E., & Newman, D. K. (2007). Biosynthesis of 2-methylbacteriohopanepolyols by an anoxygenic phototroph. *PNAS*, *104*, 15099–15104.

Reinhard, C. T., Raiswell, R., Scott, C., Anbar, A. D., & Lyons, T. W. (2009). A late Archean sulfidic sea stimulated by early oxidative weathering of the continents. *Science*, *326*, 713–716.

Ricci, J. N., Coleman, M. L., Welander, P. V., Sessions, A. L., Summons, R. E., Spear, J. R., & Newman, D. K. (2014). Diverse capacity for 2-methylhopanoid production correlates with a specific ecological niche. *The ISME Journal*, *8*(3), 675–684.

Robert, F., & Chaussidon, M. (2006). A palaeotemperature curve for the Precambrian oceans based on silicon isotopes in cherts. *Nature*, *443*, 969–972.

Rubinstein, I., Sieskind, O., & Albrecht, P. (1975). Rearranged sterenes in a shale: Occurrence and simulated formation. *Journal of the Chemical Society, Perkin Transactions*, *1*, 1833–1836.

Schoell, M., Hwang, R. J., Carlson, R. M. K., & Welton, J. E. (1994). Carbon isotopic composition of individual biomarkers in gilsonites (Utah). *Organic Geochemistry*, *21*, 673–683.

Schoell, M., McCaffrey, M. A., Fago, F. J., & Moldowan, J. M. (1992). Carbon isotopic compositions of 28, 30-bisnorhopanes and other biological markers in a Monterey crude oil. *Geochimica et Cosmochimica Acta*, *56*, 1391–1399.

Schröder, S., & Grotzinger, J. P. (2007). Evidence for anoxia at the Ediacaran-Cambrian boundary: The record of redox-sensitive trace elements and rare earth elements in Oman. *Journal of the Geological Society of London*, *164*, 175–187.

Schröder, S., Grotzinger, J. P., Amthor, J. E., & Matter, A. (2005). Carbonate deposition and hydrocarbon reservoir development at the Precambrian-Cambrian boundary: The Ara Group in South Oman. *Sedimentary Geology*, *180*, 1–28.

Schröder, S., Schreiber, B. C., Amthor, J. E., & Matter, A. (2003). A depositional model for the terminal Neoproterozoic-Early Cambrian Ara Group evaporites in south Oman. *Sedimentology*, *50*, 879–898.

Schröder, S., Schreiber, B. C., Amthor, J. E., & Matter, A. (2004). Stratigraphy and environmental conditions of the terminal Neoproterozoic-Cambrian Period in Oman: Evidence from sulphur isotopes. *Journal of the Geological Society of London*, *161*, 489–499.

Seifert, W. K., & Moldowan, J. M. (1978). Applications of steranes, terpanes and monoaromatics to the maturation, migration and source of crude oils. *Geochimica et Cosmochimica Acta*, *42*, 77–95.

Seifert, W. K., & Moldowan, J. M. (1980). The effect of thermal stress on source-rock quality as measured by hopane stereochemistry. *Physics and Chemistry of the Earth*, *12*, 229–237.

Shahar, A., & Young, E. D. (2007). Astrophysics of CAI formation as revealed by silicon isotope LA-MC-ICPMS of an igneous CAI. *Earth and Planetary Science Letters*, *257*, 497–510.

Shen, Y., & Schidlowski, M. (2000). New C isotope stratigraphy from southwest China: Implications for the placement of the Precambrian-Cambrian boundary on the Yangtze Platform and global correlations. *Geology*, *28*, 623–626.

Shiea, J., Brassell, S. C., & Ward, D. M. (1990). Mid-chain branched mono- and dimethyl alkanes in hot spring cyanobacterial mats: A direct biogenic source for branched alkanes in ancient sediments? *Organic Geochemistry*, *15*, 223–231.

Sinninghe Damsté, J. S., Van Duin, A. C. T., Hollander, D., Kohnen, M. E. L., & De Leeuw, J. W. (1995). Early diagenesis of bacteriohopanepolyol derivatives: Formation of fossil homohopanoids. *Geochimica et Cosmochimica Acta*, *59*, 5141–5157.

Sperling, E. A., Halverson, G. P., Knoll, A. H., Macdonald, F. A., & Johnston, D. T. (2013). A basin redox transect at the dawn of animal life. *Earth and Planetary Science Letters*, *371*, 143–155.

Summons, R. E., Jahnke, L. L., Hope, J. M., & Logan, G. A. (1999). 2-Methylhopanoids as biomarkers for cyanobacterial oxygenic photosynthesis. *Nature*, *400*, 554–557.

Summons, R. E., Powell, T. G., & Boreham, C. J. (1988). Petroleum geology and geochemistry of the Middle Proterozoic McArthur Basin, Northern Australia: III. Composition of extractable hydrocarbons. *Geochimica et Cosmochimica Acta*, *52*, 1747–1763.

Thunell, R. C., Tappa, E., & Anderson, D. M. (1995). Sediment fluxes and varve formation in Santa Barbara Basin, offshore California. *Geology*, *23*, 1083–1086.

Valentine, J. W. (2002). Prelude to the Cambrian explosion. *Annual Review of Earth and Planetary Sciences*, *30*, 285–306.

Volkman, J. K., Barrett, S. M., Dunstan, G. A., & Jeffrey, S. (1994). Sterol biomarkers for microalgae from the green algal class Prasinophyceae. *Organic Geochemistry*, *21*, 1211–1218.

Wang, J., Chen, D., Wang, D., Yan, D., Zhou, X., & Wang, Q. (2012). Petrology and geochemistry of chert on the marginal zone of Yangtze Platform, western Hunan, South China, during the Ediacaran-Cambrian transition. *Sedimentology*, *59*, 809–829.

Webster, N. S., Wilson, K. J., Blackall, L. L., & Hill, R. T. (2001). Phylogenetic diversity of bacteria associated with the marine sponge Rhopaloeides odorabile. *Applied and Environmental Microbiology*, *67*, 434–444.

Wille, M., Nägler, T. F., Lehmann, B., Schröder, S., & Kramers, J. D. (2008). Hydrogen sulphide release to surface waters at the Precambrian/Cambrian boundary. *Nature*, *453*, 767–769.

Wille, M., Sutton, J., Ellwood, M. J., Sambridge, M., Maher, W., Eggins, S., & Kelly, M. (2010). Silicon isotopic fractionation in marine sponges: A new model for understanding silicon isotopic variations in sponges. *Earth and Planetary Science Letters*, *292*, 281–289.

Xiao, S., & Laflamme, M. (2009). On the eve of animal radiation: Phylogeny, ecology and evolution of the Ediacara biota. *Trends in Ecology & Evolution*, *24*, 31–40.

Xiao, S., Yuan, X., & Knoll, A. H. (2000). Eumetazoan fossils in terminal Proterozoic phosphorites? *PNAS*, *97*, 13684–13689.

Yee, N., Phoenix, V. R., Konhauser, K. O., Benning, L. G., & Ferris, F. G. (2003). The effect of cyanobacteria on silica precipitation at neutral pH: Implications for bacterial silicification in geothermal hot springs. *Chemical Geology*, *199*, 83–90.

Yin, Z., Zhu, M., Davidson, E. H., Bottjer, D. J., Zhao, F., & Tafforeau, P. (2015). Sponge grade body fossil with cellular resolution dating 60 Myr before the Cambrian. *PNAS*, *112*, E1453–E1460.

Zehr, J. P. (2011). Nitrogen fixation by marine cyanobacteria. *Trends in Microbiology*, *19*, 162–173.

Ziegler, K., Young, E. D., Schauble, E. A., & Wasson, J. T. (2010). Metal–silicate silicon isotope fractionation in enstatite meteorites and constraints on Earth's core formation. *Earth and Planetary Science Letters*, *295*, 487–496.

SUPPORTING INFORMATION

Additional Supporting Information may be found online in the supporting information tab for this article.

How to cite this article: Stolper DA, Love GD, Bates S, et al. Paleoecology and paleoceanography of the Athel silicilyte, Ediacaran–Cambrian boundary, Sultanate of Oman. *Geobiology*. 2017;00:1–26. https://doi.org/10.1111/gbi.12236